

Simulating the wave-induced response of a submerged wave-energy converter using a non-hydrostatic wave-flow model

Dirk P. Rijnsdorp^{a,b,c,*}, Jeff E. Hansen^{c,d}, Ryan J. Lowe^{a,c}

^a Ocean Graduate School, University of Western Australia, Crawley 6009, WA, Australia

^b Centre for Offshore Foundation Systems, University of Western Australia, Crawley 6009, WA, Australia

^c UWA Oceans Institute, University of Western Australia, Crawley 6009, WA, Australia

^d School of Earth Sciences, University of Western Australia, Crawley 6009, WA, Australia

ARTICLE INFO

Keywords:

Wave energy
Wave energy converter
WEC
Point absorber
Non-hydrostatic
SWASH

ABSTRACT

With the increasing interest in wave energy, and when moving towards commercial-scale wave-energy projects, a detailed understanding of the interactions between single and arrays of wave-energy converters (WECs) with the ambient wave and flow field becomes imperative for both design and operational purposes, as well as assessment of their environmental impacts. This work presents a new numerical approach to simulate the nonlinear evolution of the waves and their interactions with a submerged wave-energy converter at the scale of a realistic coastal region. The numerical approach is based on the non-hydrostatic framework, and implemented in the open-source SWASH model, which provides an efficient tool to simulate the nonlinear evolution of waves over realistic coastal bathymetries. Here, we present a numerical extension to the non-hydrostatic approach to account for interactions between waves and a submerged point absorber, and to capture the response of such a wave energy device. Model results are compared with an analytical solution based on potential flow theory, a CFD simulation, and experimental data to validate its capabilities in simulating the wave-WEC interactions for both linear and nonlinear wave conditions. Overall, the results of this validation demonstrate that the model captures the wave-structure interactions and the body response with satisfactory accuracy. Notably, the results also indicate that a coarse vertical resolution was sufficient to capture these dynamics, making the model sufficiently computationally efficient to simulate the interaction of waves and WECs over large scales. As a consequence, this new modelling approach should provide a promising new alternative to simulate the interactions between nonlinear wave fields and submerged point absorbers at the scale of a realistic coastal region.

1. Introduction

Ocean waves provide a vast marine energy source that has the potential to contribute to the future renewable energy mix. To harness the power of the waves, numerous types of Wave Energy Converters (WECs) have been and are currently under development. Despite a vast number of different technologies, all designs require a large number of devices, arranged in a so-called wave farm, to extract a substantial amount of energy.

Wave farms of considerable size (say 10 to 100 devices) will likely alter both the wave field and circulation patterns in their vicinity. Devices that are arranged in arrays will also interact with each other through both scattered and radiated waves. This can subsequently impact the power generated by the individual devices, known as the “park effect” (e.g., Babarit, 2013), whereby the power take-off of N devices will not necessarily be equal to N times the power take-off of a solitary

device. Furthermore, the disturbance of wave and current fields can also potentially alter the natural conditions in the coastal zone (e.g., causing erosion or accretion of adjacent beaches), and adversely affect recreational activities (e.g., surfing) in surrounding areas. Adverse environmental effects thereby pose considerable risks in terms of financial costs for wave energy developers, and can also damage the public perception of a wave farm and wave energy more generally. A thorough understanding of both the park effect and the environmental impact is therefore of critical importance for the wave energy industry when moving towards wave farms of substantial size.

To date, no commercial-scale wave farms have been constructed, and field evidence regarding these aspects is essentially non-existent. Furthermore, laboratory studies on this subject are limited (Day et al., 2015) – apart from a few exceptions (e.g., Stratigaki et al., 2014; Özkan-Haller et al., 2017) – as they are very costly to conduct at the relevant temporal and spatial scale. Consequently, our understanding of park

* Corresponding author. Ocean Graduate School, University of Western Australia, Crawley 6009, WA, Australia.
E-mail address: dirk.rijnsdorp@uwa.edu.au (D.P. Rijnsdorp).

effects and environmental impacts by wave farms primarily relies on numerical modelling (see, for example, Wolgamot and Fitzgerald (2015) and Folley (2016) for detailed overviews of available numerical tools).

Traditionally, the local interactions between waves and floating structures have been modelled based on the potential flow equations, either solved analytically or by means of the Boundary Element Method (BEM). These techniques have also found widespread use in the wave energy community (e.g., Mavrakos and McIver, 1997; Li and Yu, 2012; Folley, 2016). They are primarily suited to resolve the details of the wave-WEC interactions (i.e., the near-field effects), and have mainly been used to study and maximise the power output of (arrays of) WECs (e.g., Wolgamot et al., 2012; Babarit et al., 2012). They are however not specifically designed to simulate the larger scale impact of WEC farms (or far-field effects), especially at the scales which are relevant when considering the environmental impact. For example, they do not account for all physical processes that are relevant to understand potential coastal impacts of wave farms (e.g., the evolution of waves over variable bathymetry, nonlinear wave interactions, and wave breaking).

For this type of application, alternative methods have been developed. The most commonly applied approach to simulate how wave farms may modify coastal wave fields is based on phase-averaged (or spectral) wave models (e.g., Gonzalez-Santamaria et al., 2013; Abanades et al., 2014; Iglesias and Carballo, 2014; Bergillos et al., 2018). With spectral wave models, the spatial and temporal evolution of the statistical properties of a wave field are modelled through the wave action balance equation, including various source terms to account for wave-related processes (e.g., wind generation, nonlinear wave interactions, and wave breaking). The impact of the energy extraction by the WECs on the wave field is typically modelled as a reduction in wave energy (or wave height) in the lee of the wave farm (Millar et al., 2007; Smith et al., 2012; Chang et al., 2016), where the energy extraction can be obtained from experiments or models that resolve the wave-structure interactions (e.g., the BEM). As phase-averaged models parametrise the relevant physical processes, they thereby do not fully represent the processes that determine the wave-WEC interactions and the wave transformation in coastal waters (e.g., diffraction and nonlinear wave-wave interactions). For example, the parametrizations of the WEC energy extraction do not account for the scattering and radiation of waves by the WEC (e.g., Özkan-Haller et al., 2017). The absence of such processes may consequently result in unrealistic predictions of the environmental impact of wave farms.

As an alternative, several studies proposed the use of a phase-resolving wave model to simulate the disturbance of the wave field by a wave farm (e.g., Beels et al., 2010a; b; Greenwood et al., 2016; Troch and Stratigaki, 2016). With the most advanced version of this approach (Troch and Stratigaki, 2016; Verbrugge et al., 2017), the impact of the wave farm on the wave field is modelled combining a BEM code to simulate the wave-structure interactions, and a phase-resolving wave model based on the potential flow equations to simulate the evolution of the waves on coastal scales (either through the mild-slope equations, Radder and Dingemans, 1985, or fully nonlinear potential flow theory, Engsig-Karup et al., 2009). In this manner, the model aims to resolve the relevant physical processes in the vicinity of the device (e.g., the radiation of waves by the motions of the WEC), and the wave processes that act on larger scales (e.g., shoaling and diffraction). However, this approach relies on the coupling with a linear wave-structure interaction model, formally restricting this method to small wave amplitudes. Furthermore, simulating the impacts of wave farms on the nearshore circulation patterns that drive the shoreline response (i.e., the erosion or accretion of a beach) will require a coupling between this approach and a circulation model.

For more extreme wave conditions, Computational Fluid Dynamic (CFD) models are better suited to simulate the wave-WEC interactions (e.g., Agamloh et al., 2008; Chen et al., 2017; Crespo et al., 2017; Ransley et al., 2017; Bharath et al., 2018; Devolder et al., 2018). Such

models can resolve the detailed turbulent flow field around the WEC, and can ideally account for all relevant physical processes that affect the wave-structure interactions. Given their detail, they require considerable computational resources which restricts their application to small spatial and temporal scales, and consequently to a single or small number of devices. CFD models are therefore at present not suited to resolve the impact of WEC farms at the spatial and temporal scales of interest.

In this work we pursue an alternative approach to numerically simulate the impact of WECs on the incident wave field, including the park effects and downstream environmental impacts of wave farms, at both relatively large scales (i.e., the nonlinear evolution of the waves over variable bathymetry and the wave-induced currents) and small scale (i.e., the wave-structure interactions). Our numerical methodology is based on the non-hydrostatic approach (e.g., Yamazaki et al., 2009; Ma et al., 2012; Ai and Jin, 2012), and implemented in the non-hydrostatic wave-flow model SWASH¹ (Zijlema et al., 2011). Non-hydrostatic wave-flow models have become a popular tool to simulate the nonlinear wave evolution and wave-induced currents in nearshore regions due to their efficiency in resolving these dynamics at coastal scales (e.g., Rijnsdorp et al., 2015, 2017; Gomes et al., 2016; García-Medina et al., 2017, and many others).

This paper present a new extension to the non-hydrostatic approach to account for the interactions between the waves and a single submerged point absorber (Section 2 and 3). To demonstrate the capabilities of the approach in simulating these interactions and the wave-induced response of the submerged device, model predictions are compared to an analytical solution based on potential flow theory for linear waves, and laboratory and numerical experiments for nonlinear wave conditions (Section 4). This work thereby provides the first step towards simulating the interactions between the waves and a WEC at the scale of a realistic coastal region using a non-hydrostatic wave-flow model (Section 5–6). Although the present work focuses on submerged point absorber devices, we envision that the numerical approach can be expanded to include other devices (e.g., floating point absorbers, bottom-mounted flaps, and oscillating water columns), pushing our modelling capabilities towards accurate predictions of large-scale impacts by arrays of generic WECs.

2. Governing equations

2.1. Fluid motion

The governing equations of the model are the Reynolds-Averaged Navier-Stokes equations for an incompressible fluid of constant density ρ . The fluid is bounded by the bottom $z = -d(x, y)$, the free-surface $z = \zeta(x, y, t)$, and a submerged obstacle with its top and bottom at $z = -S_t(x, y, t)$ and $z = -S_b(x, y, t)$, respectively; where t is time and $\langle x, y, z \rangle$ are the Cartesian coordinates (see Fig. 1). Using the Einstein summation convention, the governing equations are,

$$\frac{\partial u_j}{\partial x_j} = 0, \quad (1)$$

$$\frac{\partial u_i}{\partial t} + \frac{\partial u_i u_j}{\partial x_j} + \frac{\partial p}{\partial x_i} + g_i = \frac{\partial \tau_{ij}}{\partial x_j}, \quad (2)$$

where i and j are equal to $\langle 1, 2, 3 \rangle$, with $\langle x_1, x_2, x_3 \rangle = \langle x, y, z \rangle$, g_i represents the contribution of the gravitational acceleration $\langle 0, 0, g \rangle$, u_i is the velocity component of \vec{u} in the x_i direction, τ_{ij} represents the turbulent stresses (which are estimated based on the eddy viscosity approximation), and p is the total pressure normalised by the reference density ρ . The total normalised pressure is defined as

¹ Simulating WAVes till SHore, available under the GNU GPL license at <http://swash.sourceforge.net/>.

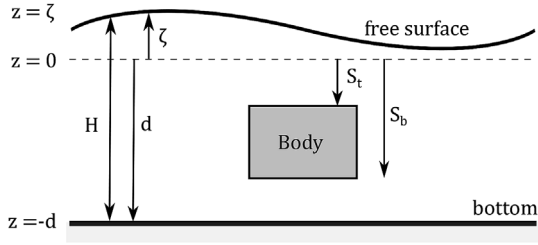


Fig. 1. Sketch of the numerical domain, including the free-surface, a submerged body, and the bottom.

$p = \rho g(\zeta - z) + \rho q$; in which the first term represents the hydrostatic pressure, and q is the non-hydrostatic pressure.

Assuming that the vertical boundaries are a single valued function of the horizontal coordinates, the following kinematic conditions apply at the free-surface and the (immobile and impermeable) bottom,

$$w \Big|_{z=\zeta} = \frac{\partial \zeta}{\partial t} + u \frac{\partial \zeta}{\partial x} + v \frac{\partial \zeta}{\partial y}, \quad (3)$$

$$w \Big|_{z=-d} = -u \frac{\partial d}{\partial x} - v \frac{\partial d}{\partial y}. \quad (4)$$

With the inclusion of a submerged body within the fluid, additional kinematic boundary conditions are introduced at the interface between the fluid and the object, where the fluid velocity equals the body velocity,

$$\mathbf{u} \cdot \mathbf{n} = \left(\frac{\partial \mathbf{X}}{\partial t} + \frac{\partial \Theta}{\partial t} \times (\mathbf{r} - \mathbf{r}_c) \right) \cdot \mathbf{n}, \quad (x, y, z) \in \mathcal{S} \quad (5)$$

where $\mathbf{u} = \langle u, v, w \rangle$ are the flow velocities, $\mathbf{X} = \langle X, Y, Z \rangle$ are the displacements of the body in x_i direction, $\Theta = \langle \theta_x, \theta_y, \theta_z \rangle$ are the rotations of the body in x_i direction, \mathbf{n} is the unit vector normal to the body surface \mathcal{S} , \mathbf{r} is the position vector, and \mathbf{r}_c is the position vector of the centre of gravity of the body. The motions of the body are governed by the rigid body equations, which will be presented in Section 2.2.

The temporal evolution of the free-surface is described by the global continuity equation, which is derived by integrating the local continuity Eq. (1) over the water column and applying the kinematic boundary conditions (Eqs. (3)–(5)),

$$\frac{\partial \zeta}{\partial t} + \int_{-d}^{\zeta} u dz + \int_{-d}^{\zeta} v dz = 0. \quad (6)$$

To complete the set of equations, boundary conditions are required at all boundaries of the domain (e.g., the free-surface, the bottom, and the horizontal boundaries). At the free-surface, we neglect the influence of viscous stresses and the influence of surface tension. Assuming that

the atmospheric pressure is constant and equal to zero (for simplicity), the non-hydrostatic pressure is set to zero at the free-surface (e.g., Stelling and Zijlema, 2003). At the bottom, the vertical velocity is imposed based on the kinematic boundary condition (Eq. (4)), and two tangential stresses (in x and y -direction, respectively) are specified to account for bottom friction. Similarly, the horizontal and vertical velocities along the body surface are computed following the kinematic boundary condition (Eq. (5)). We further assume that the submerged body is smooth, and thereby neglect the tangential stresses at its surface. Horizontal velocities are prescribed at the lateral boundaries of the domain (e.g., to generate waves or replicate closed boundaries). Finally, a combination of the $k - \epsilon$ (Lauder and Spalding, 1974) and Smagorinsky-type approximation (Smagorinsky, 1963) is used to compute the eddy viscosities (see Rijnsdorp et al., 2017, for more details).

2.2. Body motion

In this work we consider a submerged body that is restrained by an arbitrary number of tethers, see Fig. 2 for an example with one (Fig. 2a) and three taut tethers (Fig. 2b) that each include a power take-off (PTO) unit. The motions of the submerged body constrained by an arbitrary number of tethers are described following Newton's second law,

$$m \frac{\partial^2 \mathbf{X}}{\partial t^2} = \mathbf{F}, \quad (7)$$

$$\mathbf{I} \frac{\partial^2 \Theta}{\partial t^2} = \mathbf{M}, \quad (8)$$

where \mathbf{X} and Θ describe the translations and rotations of the rigid body with respect to its centre of gravity, respectively, m is the mass of the body, and $\mathbf{I} = \langle I_x, I_y, I_z \rangle$ represents the moments of inertia. Furthermore, $\mathbf{F} = \langle F_x, F_y, F_z \rangle$ and $\mathbf{M} = \langle M_x, M_y, M_z \rangle$ represent the net external forces and moments acting on the body with respect to its centre of mass, respectively.

The external forces and moments are a combination of both hydrodynamic contributions, and the contributions of the mooring lines. The hydrodynamic contributions follow from integrating the (moments of) pressure over the surface of the body \mathcal{S} ,

$$\mathbf{F}_h = \iint_{\mathcal{S}} p \mathbf{n} d\mathcal{S}, \quad (9)$$

$$\mathbf{M}_h = \iint_{\mathcal{S}} (\mathbf{r} - \mathbf{r}_c) p \mathbf{n} d\mathcal{S}. \quad (10)$$

The forces and moments induced by the tethers and PTO units depend on the mooring configuration of the submerged body. In this study, we model the influence of the tether and the PTO system as a linear spring damper (e.g., Babarit et al., 2012; Alves, 2016; Sergiienko et al., 2017). In this case, the force induced by each tether at its

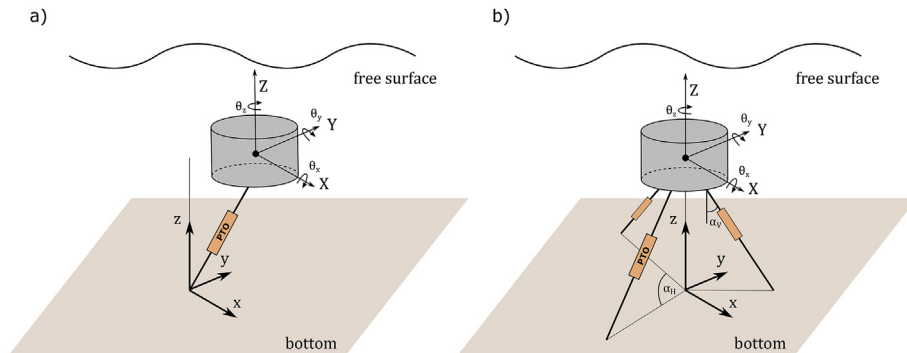


Fig. 2. Sketch of a submerged body that is moored by one (panel a) and three tethers (panel b), each including a power take-off (PTO) unit. For the three-tethered device (panel b), the tethers are equally distributed around the buoy (with an angle of $\alpha_H = 120^\circ$ between the tethers), point towards the centre of gravity, and are inclined to the vertical at angle α_V .

attachment point to the body is given by,

$$F_l = -\mathbf{n}_l \left(C + K_{pto} l + B_{pto} \frac{\partial l}{\partial t} \right), \quad (11)$$

where \mathbf{n}_l is the unit vector normal to the line attachment point, C is the pretension of a tether to counteract the buoyancy force, l is the linear displacement of the tether, and B_{pto} and K_{pto} are the damping and spring coefficient of the PTO unit, respectively. Although this work only considers the PTO to act as a linear spring damper, this can easily be extended with any other mathematical formulation that mimics the PTO behaviour. For example, end stop forces (e.g., Babarit et al., 2012) can be included to control the maximum stroke of the PTO.

3. Numerical implementation

The fluid domain is divided into K terrain-following layers in the vertical direction, and into cells with a resolution of Δx and Δy in the x and y directions, respectively. Away from the object, the spatially-varying layer thickness is computed as $h_k = f_k(\zeta + d)$, where f_k indicates the relative thickness of each layer (i.e., $0 < f_k \leq 1$ and $\sum_{k=1}^K f_k = 1$). To accommodate the submerged obstacle within the grid, a body conforming grid is used for the cells that include the obstacle. In this region, the cells are divided into three regions: above, inside, and below the obstacle; where the layer thickness is determined as,

$$h_k = \frac{\zeta + S_t}{k_{S_t}}, \quad k \leq k_{S_t}, \quad (12)$$

$$h_k = \frac{S_t - S_b}{k_{S_b} - k_{S_t} - 1}, \quad k_{S_t} < k < k_{S_b}, \quad (13)$$

$$h_k = \frac{d - S_b}{K - k_{S_b} + 1}, \quad k \geq k_{S_b}, \quad (14)$$

where k_{S_t} and k_{S_b} indicate the layer above and below the obstacle, respectively, S_t is the distance from the surface to the top of the body, and S_b is the distance from the bottom of the body to the bottom (Fig. 3). To ensure a smooth transition between the two grid layering systems, we use an overlapping region with a width equal to the body diameter in which a linearly varying layer thickness smoothly connects the two grid systems. The flow grid is updated every time step to accommodate for the motions of the free surface and the obstacle. With respect to the latter, we only accounted for the heave motion when updating the fluid grid (which will be discussed in further detail below).

The velocity components are positioned on the grid using a staggered arrangement and the free surface is located at the centres of a cell, as illustrated in Fig. 3. Following Rijnsdorp and Zijlema (2016), the non-hydrostatic pressure is positioned at the vertical interfaces of a cell

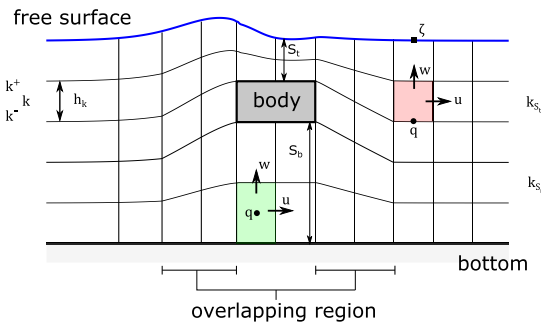


Fig. 3. Sketch of the horizontal and vertical grid schematisation, and the staggered variable arrangement on the grid. The variable arrangement is depicted for cells above and away for the body (illustrated in the red control volume), and for cells underneath the body (illustrated by the green control volume). (For interpretation of the references to color in this figure legend, the reader is referred to the Web version of this article.)

above and away from the body, whereas it is positioned at the centre of a cell underneath the body. In this manner, we can adopt the Keller-Box scheme (Lam and Simpson, 1976; Stelling and Zijlema, 2003) to efficiently resolve the dispersive properties of the free-surface waves, and the (traditional) cell-centred arrangement (e.g., Stansby and Zhou, 1998; Casulli and Stelling, 1998) which allows for an easier implementation in the pressurised region underneath the body (where the celerity is infinite).

With this implementation, the body is directly included in the fluid domain, and the relevant kinematic boundary conditions can be directly applied at the fluid-structure interfaces. Furthermore, the use of a terrain-following coordinate system for the z -direction permits a straightforward inclusion of its heaving motion. However, significant horizontal body motions and rotations can not be straightforwardly included without altering the horizontal grid structure (or using an immersed boundary type method). Although this is a limitation of our implementation, we wish to keep the numerical method as simple and efficient as possible and, therefore, tentatively assume that the horizontal motions and rotations are small with respect to the fluid grid. Thus, we neglect these motions of the body within the fluid grid. Although this formally restricts the approach to relatively small body motions and rotations, we demonstrate how our methodology still adequately replicates the body response in nonlinear wave conditions (see Section 4.3.2).

In the following (Section 3.1–3.3), we present the methodology to solve the governing equations on the numerical grid. To keep a concise description, the equations are presented in a semi-discrete form which is obtained by discretising the vertical dimensions, while retaining a continuous description for the horizontal coordinates and time. Furthermore, we omitted the turbulent stresses from the description below as the implementation of the turbulent terms are not affected by the inclusion of a submerged obstacle.

3.1. Fluid motion

The position of the free-surface is governed by the global continuity equation (6). In semi-discretised form, a global mass conserving discretisation of this equation is,

$$\frac{\partial \zeta}{\partial t} + \sum_{k=1}^K \left[\frac{\partial h_k u_k}{\partial x} + \frac{\partial h_k v_k}{\partial y} \right] = 0, \quad (15)$$

where u_k and v_k is the layer-averaged velocity in layer k in the x and y direction. A local mass conserving equation is derived by integrating the local continuity equation over a layer k (i.e., over $z_k^- \leq z \leq z_k^+$),

$$\begin{aligned} \frac{\partial h_k u_k}{\partial x} + \frac{\partial h_k v_k}{\partial y} + w_{k^+} - w_{k^-} - \bar{u}_{k^+} \frac{\partial z_{k^+}}{\partial x} + \bar{u}_{k^-} \frac{\partial z_{k^-}}{\partial x} - \bar{v}_{k^+} \frac{\partial z_{k^+}}{\partial y} \\ + \bar{v}_{k^-} \frac{\partial z_{k^-}}{\partial y} = 0, \end{aligned} \quad (16)$$

where z_{k^\pm} are the vertical layer interfaces of a cell, and the overline indicates that the respective variable (e.g., \bar{u}_{k^\pm}) is computed by means of linear interpolation.

To compute the temporal variation of the vertical velocity field, the vertical momentum Eq. (2) is first integrated over $z_k \leq z \leq z_{k+1}$. In semi-discretised form, the resulting equation is,

$$\begin{aligned} \frac{\partial h_{k^+} w_{k^+}}{\partial t} + \frac{\partial h_{k^+} \bar{u}_{k^+} w_{k^+}}{\partial x} + \frac{\partial h_{k^+} \bar{v}_{k^+} w_{k^+}}{\partial y} + \hat{w}_{k+1} \bar{\omega}_{k+1} - \hat{w}_k \bar{\omega}_k \\ = -h_{k^+} \left\langle \frac{\partial q}{\partial z} \right\rangle_{z_{k^+}}. \end{aligned} \quad (17)$$

in which the turbulent terms are omitted for brevity. Here, the brackets indicate averaging over a w -velocity layer, $\langle \dots \rangle_{z_{k^+}} = \frac{1}{z_{k+1} - z_k} \int_{z_k}^{z_{k+1}} \dots dz$, and ω is the relative vertical velocity which is defined as,

$$\omega_{k^+} = w_{k^+} \frac{\partial z_{k^+}}{\partial t} - \bar{u}_{k^+} \frac{\partial z_{k^+}}{\partial x} - \bar{v}_{k^+} \frac{\partial z_{k^+}}{\partial y}. \quad (18)$$

Furthermore, the hat indicates that the respective variable (in this case the flux-transported vertical momentum) is computed using an appropriate flux-limited interpolation (e.g., Zijlema et al., 2011).

In a similar fashion, the temporal variation of the horizontal velocity field is computed based on the horizontal momentum Eq. (2), after integrating over $z_k^- \leq z \leq z_{k^+}$. For example, the u -momentum equation in semi-discretised form is (again omitting the turbulent terms for brevity),

$$\begin{aligned} \frac{\partial h_k u_k}{\partial t} + \frac{\partial h_k u_k^2}{\partial x} + \frac{\partial h_k v_k u_k}{\partial y} + \hat{u}_{k^+} \omega_{k^+} - \hat{u}_{k^-} \omega_{k^-} \\ = -g h_k \frac{\partial \zeta}{\partial x} - h_k \left\langle \frac{\partial q}{\partial x} \right\rangle_{z_k}, \end{aligned} \quad (19)$$

where the brackets indicate averaging over a u -velocity layer,

$$\langle \dots \rangle_{z_k} = \frac{1}{z_{k^+} - z_k^-} \int_{z_k^-}^{z_{k^+}} \dots dz.$$

In these semi-discretised momentum equations, the non-hydrostatic pressure gradient is not evaluated. As mentioned previously, a pressure variable is positioned at the vertical cell face when a cell is located away or above the obstacle, and it is positioned in the cell centre if the cell is located underneath the obstacle. In case of the vertical momentum equation, the non-hydrostatic pressure term is discretised using standard central differences when a cell is located underneath the obstacle,

$$\left\langle \frac{\partial q}{\partial z} \right\rangle_{z_{k^+}} = \frac{q_{k+1} - q_k}{h_{k^+}}. \quad (20)$$

In contrast, this term is discretised using the Hermetian relation when a cell is located away or above the obstacle (e.g., Rijnsdorp and Zijlema, 2016),

$$\left\langle \frac{\partial q}{\partial z} \right\rangle_{z_{k^+}} + \left\langle \frac{\partial q}{\partial z} \right\rangle_{z_k^-} = 2 \frac{q_{k^+} - q_k^-}{h_k}. \quad (21)$$

For the u -momentum equation, the non-hydrostatic pressure term is evaluated as follows (and in a similar fashion for the v -momentum equation),

$$\left\langle \frac{\partial q}{\partial x} \right\rangle_{z_k} = \begin{cases} \frac{1}{h_k} \left(\frac{\partial h_k \bar{q}_k}{\partial x} - q_{k^+} \frac{\partial z_{k^+}}{\partial x} + q_k^- \frac{\partial z_k^-}{\partial x} \right) & \text{(Above and away from the obstacle),} \\ \frac{1}{h_k} \left(\frac{\partial h_k \bar{q}_k}{\partial x} - \bar{q}_{k^+} \frac{\partial z_{k^+}}{\partial x} + \bar{q}_k^- \frac{\partial z_k^-}{\partial x} \right) & \text{(Underneath the obstacle).} \end{cases} \quad (22)$$

These dynamical equations for the horizontal and vertical velocities (Eq. (17)–(19)) apply when the respective variable is located in the fluid domain. When a variable is located at the bottom boundary or at the fluid-structure interface, we impose the relevant kinematic boundary conditions (Eqs. (4) and (5)). The kinematic boundary conditions introduce the coupling between the body and the fluid motion in the flow equations.

To complete the description of the numerical model, the continuous description for time and the horizontal dimensions needs to be replaced by discrete approximations. In this work, we closely follow the original methodology of the SWASH model (Zijlema and Stelling, 2005, 2008; Zijlema et al., 2011), in which the equations are discretised on a curvilinear grid. Combined with the staggered variable arrangement, the horizontal gradients of the hydrostatic and non-hydrostatic pressure are computed using central differences. The temporal evolution of the equations is evaluated using the second-order accurate leapfrog scheme (Hansen, 1956) to couple the flow and hydrostatic pressure. This is combined with a second-order pressure correction scheme (Van Kan, 1986) to account for the non-hydrostatic pressure. The horizontal

advective terms are discretised in space and time using the second-order flux limited MacCormack scheme, in combination with the approach of Stelling and Duinmeijer (2003) to ensure proper conservation properties in case of flow contractions and flow expansions (e.g., breaking waves). To avoid small time steps in case of thin water layers, the vertical advective terms are discretised using implicit time integration schemes.

3.2. Body motion

The equations for the body motion are discretised using the Newmark scheme (Newmark, 1959). For example, the acceleration \mathbf{A} ($= \frac{\partial^2 \mathbf{X}}{\partial t^2}$), velocity \mathbf{V} ($= \frac{\partial \mathbf{X}}{\partial t}$), and translation \mathbf{X} of the submerged body are evaluated as,

$$\mathbf{A}^{n+1} = \frac{\mathbf{F}^{n+1}}{m} = \frac{\mathbf{F}_h^{n+1} + \sum_{l=1}^{N_m} \mathbf{F}_l^{n+1}}{m}, \quad (23)$$

$$\mathbf{V}^{n+1} = \mathbf{V}^n + \Delta t ((1 - \gamma) \mathbf{A}^n + \gamma \mathbf{A}^{n+1}), \quad (24)$$

$$\mathbf{X}^{n+1} = \mathbf{X}^n + \Delta t \mathbf{V}^n + \frac{1}{2} \Delta t^2 ((1 - 2\beta) \mathbf{A}^n + 2\beta \mathbf{A}^{n+1}), \quad (25)$$

where N_m is the number of tethers connected to the body, and β ($= 0 - \frac{1}{2}$) and γ ($= 0 - 1$) are the Newmark parameters that control the temporal accuracy of the solution. In this work, $\beta = \frac{1}{4}$ and $\gamma = \frac{1}{2}$ unless specified otherwise, which corresponds to the second-order accurate Newmark scheme. The rotation of the body Θ and its time derivative Φ ($= \frac{\partial \Theta}{\partial t}$) are computed in a similar fashion. The resulting system of equations determine the unknown body motions (i.e., \mathbf{X}^{n+1} , \mathbf{V}^{n+1} , Θ^{n+1} , and Φ^{n+1}).

The primary difficulty in solving this system of equations is related to the implicit contribution of the external forces and moments, which need to be evaluated at the next time step $(n + 1)\Delta t$ (e.g., \mathbf{F}^{n+1}). This mainly applies to the hydrodynamic forces and moments, which are computed as the integral of the pressure (moment) over the surface of the body, Eqs. (9) and (10). The hydrodynamic forces and moments depend on the pressure at $(n + 1)\Delta t$ (i.e., $p^{n+1} = \rho g (\zeta^{n+1} - z) + \rho q^{n+1}$), which is not yet known when solving the rigid body equations. To include this implicit part of the hydrodynamic forces, several iterations are required during each time step.

Typically, a submerged wave energy converters is positively buoyant, with a mass that is relatively small compared to its added mass. Numerous previous studies have shown that in this case a large number of iterations are required to reach convergence when solving the fluid-structure interactions (e.g., Borazjani et al., 2008; Yu et al., 2015). To overcome this, we use an under relaxation scheme when computing the body response,

$$\tilde{\mathbf{A}}_j^{n+1} = (1 - \alpha) \tilde{\mathbf{A}}_{j-1}^{n+1} + \alpha \mathbf{A}_j^{n+1}, \quad (26)$$

$$\tilde{\Theta}_j^{n+1} = (1 - \alpha) \tilde{\Theta}_{j-1}^{n+1} + \alpha \Theta_j^{n+1}, \quad (27)$$

where α is the under-relaxation parameter ($0 \leq \alpha \leq 1$), the tilde \approx indicates the under-relaxed solution, and j indicates the iteration number during a time step. For all simulations in this work, the under-relaxation parameter was set as $\alpha = 0.3$.

3.3. Fluid-structure coupling and solution algorithm

The kinematic boundary conditions at the hull of the submerged body (Eq. (5)) and the integral of the pressure (moments) over this surface (Eqs. (9) and (10)) provide the coupling between the fluid motion and the body response. As the fluid motions depend on the body motions, and the body motions depend on the fluid pressure, an iterative technique is required to solve the governing equations (as discussed in Section 3.2).

We use the following solution algorithm to iteratively solve the set of equations that comprise the fluid and body dynamics.

1. Begin the computation with the fluid variables (ζ^n, u_i^n, q^n), and body motions ($\mathbf{X}^n, \mathbf{V}^n, \Theta^n, \Phi^n$) from the initial conditions or the previous time step.
2. Compute the fluid motion
 - (a). Prescribe the kinematic boundary conditions, Eqs. (4) and (5), at the body surface based on the known body motions (e.g., \mathbf{V}^n if $k = 1$, and \mathbf{V}_k^{n+1} when $k > 1$).
 - (b). Solve the equations governing the fluid motion, Eq. (15)–(17), (19), to obtain ζ^{n+1}, u_i^{n+1} and q^{n+1} .
3. Compute the body motions
 - (a). Integrate the pressure over the body surface to compute the hydrodynamic forces \mathbf{F}_h^{n+1} and moments \mathbf{M}_h^{n+1} acting on the body, Eqs. (9) and (10).
 - (b). Compute the acceleration of the body for both the translational and rotational motions (e.g., Eq. (23)), and apply the under relaxation, Eqs. (26) and (27).
 - (c). Compute the body velocity and motions of the k th iteration by solving the rigid body equations (e.g., Eqs. (24) and (25)).
4. Check convergence
 - (a). Compute $\Delta \mathbf{C}_k = \begin{bmatrix} \mathbf{V}_{k+1}^{n+1} - \mathbf{V}_k^{n+1} \\ \Phi_{k+1}^{n+1} - \Phi_k^{n+1} \end{bmatrix}$ to check if the solution has converged.
 - (b). If $\|\Delta \mathbf{C}_k\|^2 < \epsilon$, advance the computation to the next time step, where ϵ is a small number. In this work, we set $\epsilon = 10^{-5}$ to ensure that convergence is reached.
 - (c). Otherwise, return to step 2a, and repeat the procedure until convergence is reached.

4. Test cases

4.1. Convergence test

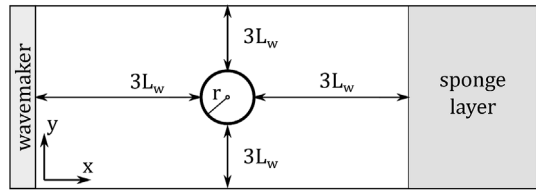
As a first test, we study the convergence of the developed model when simulating the interaction of a linear monochromatic wave (with amplitude $a = 0.005$ m and period $T = 10$ s) with a submerged cylinder (see Fig. 4 for the relevant dimensions) that is located in a numerical wave basin spanning $\sim 130 \times 740$ m (width \times length) with a constant water depth of $d = 10$ m, including a sponge layer at the eastern boundary to absorb the outgoing waves. In this test, body motions are not included and we thereby consider the interactions of the waves with a fixed submerged obstacle (known as the diffraction problem). We tested the convergence of the model for a variable horizontal and vertical grid resolution. For the horizontal convergence test, the grid resolution was varied between 10 – 50 points per cylinder diameter (resulting in $\Delta x = \Delta y = 0.3 - 2.0$ m) with a constant number of 3 layers in the vertical and a constant time step of $\Delta t = 0.016$ s. For the vertical convergence test, we used 3 – 12 layers with a constant horizontal grid resolution of $\Delta x = \Delta y = 2.0$ m and a constant time step of $\Delta t = 0.08$ s. For all simulations, 1 layer was located above the obstacle ($k_{s_1} = 1$) and 1 layer ran through the obstacle ($k_{s_2} = 3$), with the remaining layers located below the obstacle.

To quantify the model convergence, we computed the normalised root-mean-square-error (nE) of the vertical force time series \hat{F}_z (see Appendix A for its definition). For both the horizontal and vertical resolution, the nE reduced for an increasingly fine grid resolution (see Fig. 5). Fitting an exponential function through the results ($f(\Delta x) = a\Delta x^b$, where a and b are real numbers) indicates that for both grid resolutions the model converged with a rate of about $b = 1.7$.

4.2. Linear waves

To validate the model for linear waves, we compared model results

a) plan view



b) side view

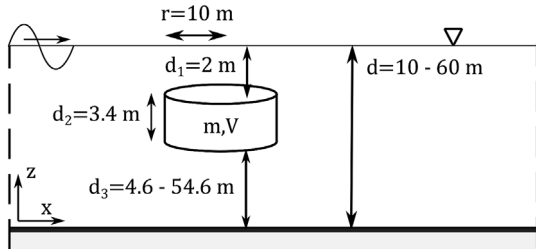


Fig. 4. Plan view (panel a) and side view (panel b) of the problem set-up (not to scale), including the relevant dimensions. In panel a, L_w is the wave length.

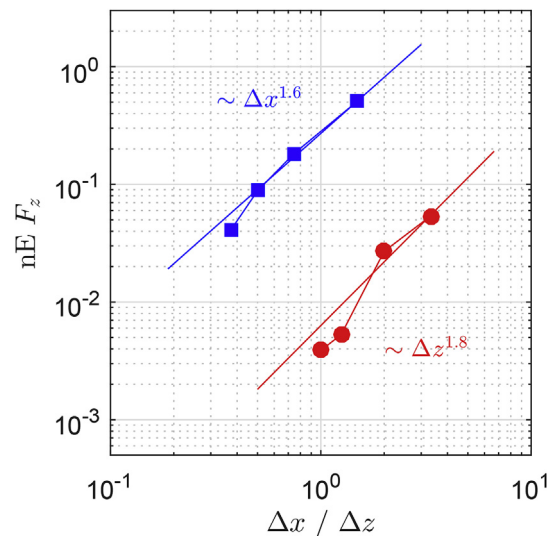


Fig. 5. Normalised root mean square error (nE) of the vertical force F_z^n for a varying horizontal (blue lines and square markers) and vertical resolution (red lines and circular markers), where $\Delta z = \frac{d}{K}$ (i.e., the layer thickness with respect to the still water depth). The straight lines illustrate exponential functions ($f(\Delta x) = a\Delta x^b$) fitted to the data points, and the text labels indicate the exponential b of the fitted functions. (For interpretation of the references to color in this figure legend, the reader is referred to the Web version of this article.)

with an analytical solution of the linearised potential flow problem for monochromatic waves interacting with a submerged cylinder. This includes a) the interactions of the waves with a non-moving obstacle (the diffraction problem), b) the radiation of waves due to forced obstacle motions (the radiation problem), and c) the fully-coupled wave-induced response of the device. We considered a range of monochromatic waves with wave periods ranging $T = 4 - 14$ s (with 1 s increments), and a cylinder with constant dimensions that is located in a water depth ranging $d = 10 - 60$ m (with 10 m increments), see Fig. 4 for the relevant dimensions and a sketch of the problem set-up for the diffraction and body response simulations. For the radiation problem we used a similar set-up, but with sponge layers located at all side boundaries of the domain to absorb the radiated waves. To facilitate a comparison with the linear potential flow theory, the amplitude of the incident

waves and the forced body motions (in the case of the radiation problem) was set to $a = 0.005$ m for all simulations. The cylinder with a volume of 1.07×10^3 m³ was positively buoyant with a density set at 240 kg m⁻³, resulting in a mass of $m = 256.8 \times 10^3$ kg and a moment of inertia of $I_y = 641.7 \times 10^3$ kg m².

For the diffraction and radiation problem, we verified the numerical predictions by comparing them with the eigenfunction expansion solution of Jiang et al. (2014a, b). With this analytical approach, eigenfunction expansions of the velocity potential are matched at each of the sub-domain interfaces (i.e., away from the cylinder, above the cylinder, and underneath the cylinder). Truncating the eigenfunction series at N yields a linear system of algebraic equations, which can be solved numerically. For this test case, we truncated the eigenfunction series at $N = 100$, for which we observed that the analytical solutions converged for all water depths that were considered (not shown). To validate the model for the wave-induced response of the submerged cylinder, model predictions were compared to a frequency domain solution of the rigid body equations based on the hydrodynamic coefficients of the potential flow solution (see Appendix B for more details).

In the 3D numerical simulations, we used a rectangular domain with horizontal domain dimensions that are a multiple of the wave length L_w , combined with sponge layers at the downwave end of the domain, to minimise the influence of wave reflections at the horizontal domain boundaries. The domain was discretised with a rectilinear grid in the horizontal directions, with the finest grid near the cylinder ($\Delta x = \Delta y \approx 1$ m, corresponding to 20 points per cylinder diameter). As we cannot perfectly reproduce a circular shape using a rectilinear grid, the grid was slightly altered to ensure that the cylinder in SWASH had the same volume as the analytical cylinder. The grid sizes increased away from the cylinder, with a maximum resolution that ensures at least 20 points per wave length. The number of vertical layers was chosen such that the aspect ratio of the horizontal versus the vertical grid resolution had a maximum of 10 away from the cylinder where equidistant layers were used (with a minimum of 3 layers). This resulted in a vertical resolution that decreased with the water depth and ranged 3 – 7 layers. For all simulations, similar to the convergence test case, only 1 layer was located above the obstacle ($k_{s,t} = 1$), 1 layer ran through the obstacle ($k_{s,b} = 3$), and the remaining layers were located below the obstacle. Each simulation was run for a duration of 10 wave periods after steady state conditions were reached. The time step was set as such to ensure that the Courant number was smaller than 0.8.

To illustrate the impact of the WEC on the wave field, Fig. 6 shows the surface elevation around a single tethered device moored at $d = 10$ m that is subject to an incident wave of $T = 4$ s. This snapshot shows how the diffracted wave field combined with the waves radiated by the body motions disturb the incident wave field in the lee of the obstacle. In the following, we will compare the model results with the potential flow solution for the diffraction and radiation problem (Section 4.2.1), and the wave-induced response of the body (Section 4.2.2). In both sections, we first discuss the results in detail for a single water depth, followed by a comparison for all 7 water depths.

4.2.1. Diffraction and radiation problem

To illustrate the agreement between the model predictions and the analytical solution, Fig. 7 shows the results for a case with $d = 30$ m for both the diffraction (Fig. 7a–c) and radiation problems (Fig. 7d–f). For the diffraction problem, the amplitude and phase (relative to the incident wave) of the vertical force (Fig. 7a), horizontal force (Fig. 7b), and moment (Fig. 7c) varied significantly as a function of the wave period T . For the range of wave periods considered, the model reproduced both the amplitude and phase of the three load components.

A similar agreement between the model predictions and analytical solution was found for the hydrodynamic coefficients of the radiation problem (Fig. 7d–e), based on the added mass A and radiation damping B coefficient (computed as the part of the force that is in phase and out of phase with the cylinder acceleration, respectively). For all three

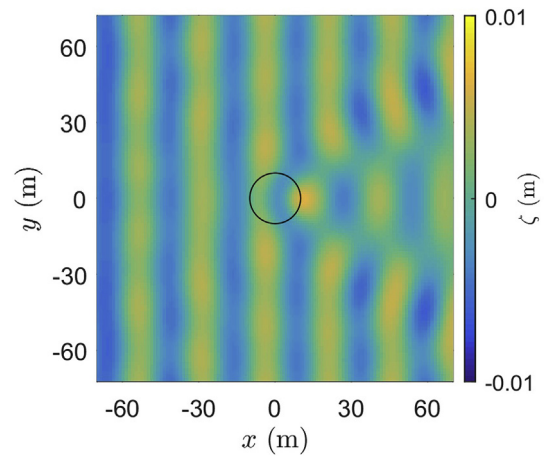


Fig. 6. Snapshot of the predicted surface elevation ζ for a dynamic response simulation of the single tethered device moored at $d = 10$ m that is subject to an incident wave with period $T = 4$ s. The location of the device is indicated by the black circle.

degrees of freedom, the predicted and analytical hydrodynamic coefficients agreed well with the analytical solution for the range of wave periods considered. This includes the negative added mass that occurred at lower wave periods for the heave (Fig. 7d) and pitch problem (Fig. 7f). Discrepancies between the predictions and analytical results appeared to be largest (but still relatively small) at lower wave periods for the added mass coefficients in heave and especially pitch.

Comparing the results for all water depths, the predicted results and the analytical solution of the diffraction problem were in excellent agreement (Fig. 8a). This was confirmed by the three statistical model performance metrics (Table 1, see Appendix A for their definition), which indicate that the hydrodynamic loads were predicted with almost perfect skill, low errors, and near zero bias. For the radiation problem, discrepancies between the model predictions and analytical solution were typically larger (Fig. 8b and Table 1). Nonetheless, the model captured the variation of all hydrodynamic coefficients for the whole range of water depths (not shown), akin the results shown in Fig. 7d–f for $d = 30$ m.

4.2.2. Wave-induced response

To validate the model for the wave-induced response of the cylinder, we compared model predictions with a frequency domain solution of the rigid body equations based on the analytical hydrodynamic coefficients (see Appendix B for additional details). We considered two mooring arrangements with the cylinder being restrained by either one or three tethers that each include a PTO system (see Fig. 2). The PTO parameters (K_{pto} and B_{pto}) were chosen such that the undamped natural frequency in heave equals $f = 0.1$ Hz. Similar to the previous section, we will first discuss the results for a single water depth in detail, followed by an overview of the results for all water depths.

The left panels of Fig. 9 show the results for the dynamic response and power take-off for the single tethered device moored at a depth of $d = 30$ m. For the range of wave periods considered, the predicted surge and heave response were in good agreement with the linear frequency domain solution (Fig. 9a and c), as the model captured their variation and typical magnitude. The agreement is confirmed by the Murphy Skill (MS) score (see Appendix A for its definition), which was $MS = 0.86$ for surge and $MS = 0.96$ for heave. In contrast, the pitch response was predicted with much poorer accuracy ($MS = -64.2$), as it was significantly over predicted for most of the wave periods and especially near $T = 12$ s (Fig. 9e). Near this wave period, the model appeared to predict a resonant pitch response, whereas the analytical model suggested a resonant response at $T = 14$ s. The discrepancies in the pitch

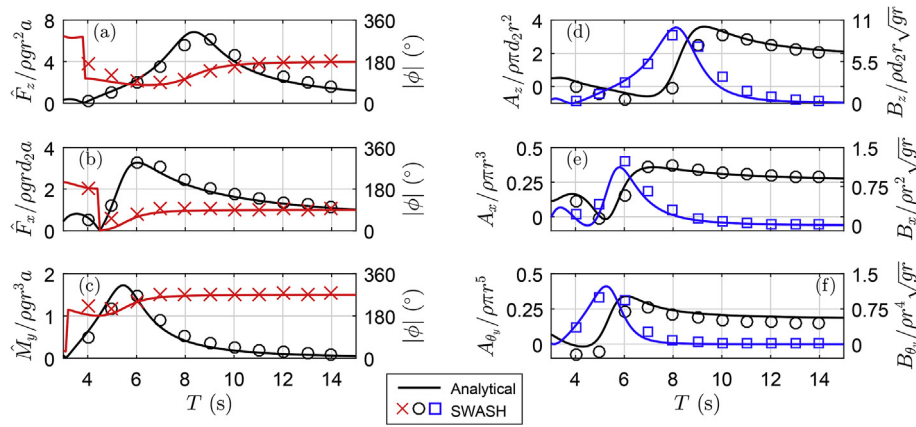


Fig. 7. Numerical predictions (markers) and analytical results (lines) of the diffraction problem (panel a–c), the radiation problem (panel d–f) for a water depth $d = 30$ m. Panel a–c: normalised hydrodynamic forces and moment that act on the cylinder (left axis – black lines and circular markers), and the phase difference between the respective load component and the incident wave signal (right axis – red lines and cross markers). Panel d–f: normalised added mass (left axis – black line and circle markers) and radiation damping (right axis – blue line and square markers) coefficient for the heave (panel d), surge (panel e), and pitch (panel f) motion. (For interpretation of the references to color in this figure legend, the reader is referred to the Web version of this article.)

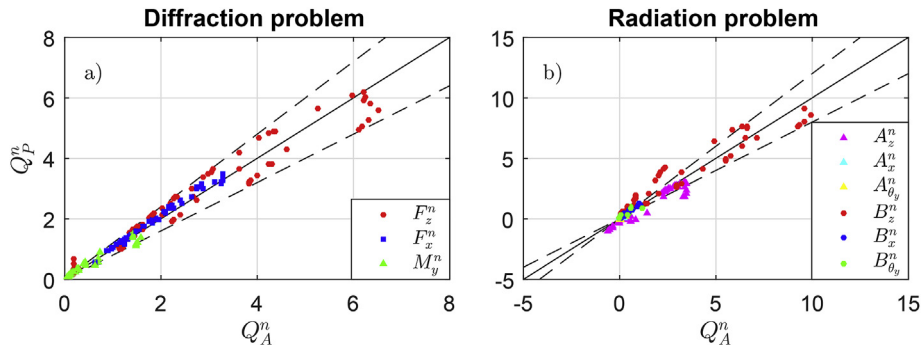


Fig. 8. Scatter plot of the numerical predictions Q_P^n versus the analytical Q_A^n results (where the superscript \dots^n indicates normalisation) for the diffraction problem (panel a), and the radiation problem (panel b) of all simulations. The black line indicates one on one correspondence, and the dashed lines indicate the 20% error bands. The colors indicate the respective degree of freedom (panel a) and hydrodynamic coefficient (panel b), as indicated in the legend of each panel. (For interpretation of the references to color in this figure legend, the reader is referred to the Web version of this article.)

response illustrate the difficulties when simulating the wave-induced response of this submerged body, which are mostly related to the resonant nature of the device. Even though the excitation force and the hydrodynamic coefficients agreed well with the analytical solution for this depth, the resulting response can still show significant discrepancies. The predicted power take-off \bar{P} however agreed well with

the analytical solution (Fig. 9g), with $MS = 0.94$. This result is consistent with the agreement in heave, as – in the linear case – \bar{P} only depends on the heave response (see Appendix B).

Typically, the overall response of the three-tethered device appears to be predicted with an accuracy that is comparable to the single tethered-device (right panels Fig. 9). Heave was predicted with the best

Table 1

Normalised root mean square error (nE), relative bias (RB), and Murphy (1988) Skill Score of the numerical predictions (see Appendix A for their definitions) for the various parameters of the diffraction problem, radiation problem, and dynamic response for all wave periods and water depths that were considered in Section 4.2

	Diffraction problem			Radiation problem					
	\hat{F}_x	\hat{F}_z	\hat{M}_y	A_x	A_z	A_{θ_y}	B_x	B_z	B_{θ_y}
nE	0.17	0.22	0.23	0.30	0.32	0.59	0.31	0.26	0.32
RB	0.05	0.00	0.01	-0.04	-0.23	-0.25	0.32	0.11	0.20
MS	0.97	0.95	0.94	0.90	0.88	0.61	0.90	0.92	0.88
Dynamic response									
1 tether				3 tethers					
\hat{X}	\hat{Z}	$\hat{\theta}_y$	\hat{P}	\hat{X}	\hat{Z}	$\hat{\theta}_y$	\hat{P}		
0.48	0.20	5.05	0.29	1.66	0.23	0.62	0.32		
-0.02	-0.04	2.82	-0.09	0.05	-0.08	-0.26	-0.14		
0.69	0.95	-35.26	0.91	-2.43	0.94	0.54	0.89		

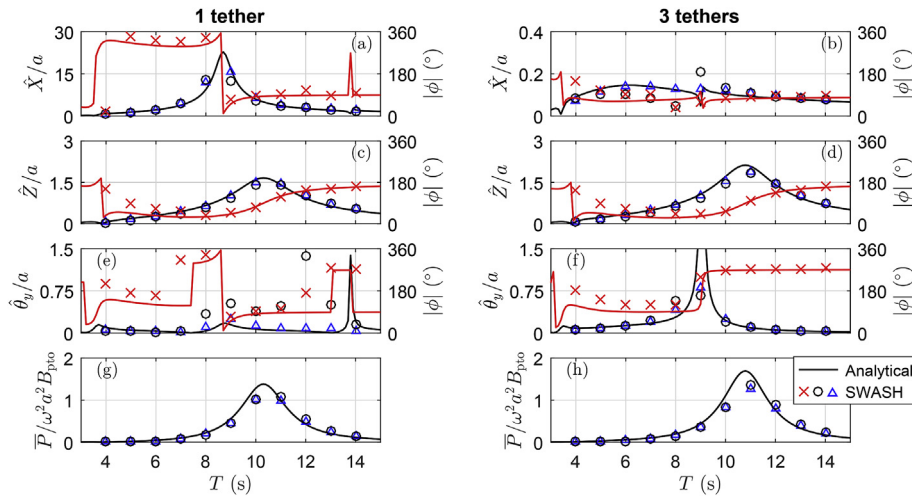


Fig. 9. Numerical predictions (makers) and analytical results (lines) for the dynamic response and the mean power take off of a single (left panels) and three tethered device (right panels) moored at a water depth of $d = 30$ m. Panel a–f: normalised surge (panel a–b), heave (panel c–d), and pitch (panel e–f) response of the cylinder (left axis) and phase difference between the respective body motion and the incident wave (right axis). Panels g–h: normalised power take off. Black markers indicate the normalised amplitudes and power take off for a 4 layer simulation, and blue markers for a 30 layer simulation. (For interpretation of the references to color in this figure legend, the reader is referred to the Web version of this article.)

skill ($MS = 0.95$), followed by pitch ($MS = 0.20$) and surge ($MS = -3.1$). Although the skill was poor for surge, the model captured the general frequency variation of the surge response (Fig. 9b). Notably, the model resolved the typical magnitude of the surge response, which was much smaller for the three-tethered device compared to the single-tethered device. Furthermore, the model captured the resonant pitch response much better than for the single tethered device, although the resonant peak appears to be predicted at a slightly lower wave period (Fig. 9f). For the three-tethered device, the power take-off depends on both the heave and the surge response (see Appendix B). Despite inaccuracies in

the predicted surge response, the predicted power take-off agreed well with the analytical solution ($MS = 0.93$).

For both mooring arrangements, discrepancies were found to reduce significantly for an increasing number of vertical layers. With 30 instead of 4 vertical layers, the predicted body motions in surge and pitch were much improved (blue versus black markers in Fig. 9). This suggests that the discrepancies are not a fundamental flaw of the numerical methodology, but are related to modelling inaccuracies due to the coarse vertical resolutions that were used in this work. On average, the runtime of the 30 layer simulations was 7 times longer compared to the

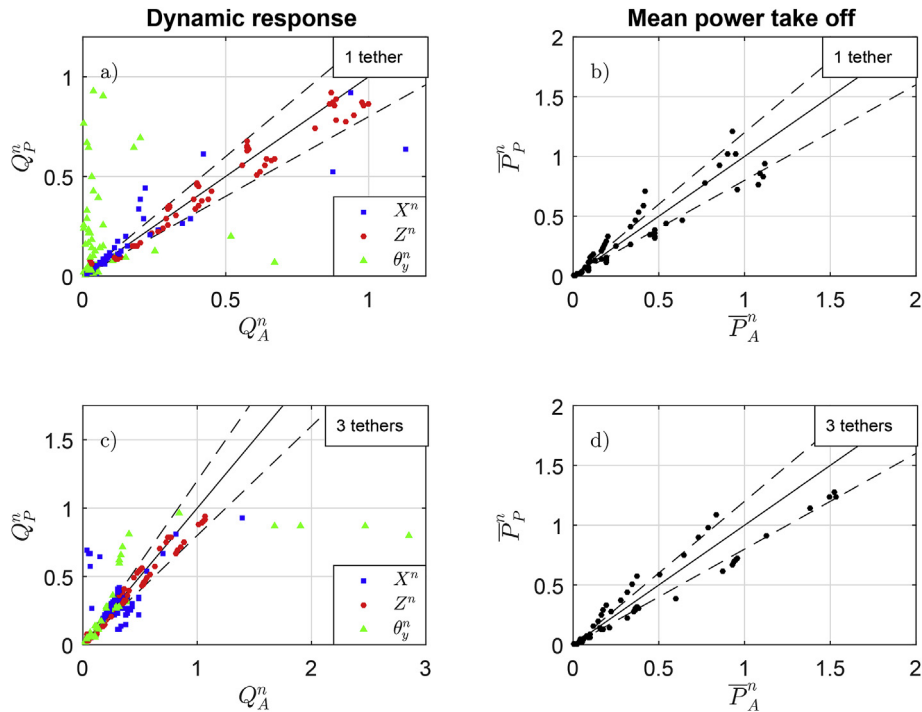


Fig. 10. Scatter plot of the numerical predictions (subscript \dots_P) versus the analytical results (subscript \dots_A) for the normalised body response (panel a and c), and the normalised mean power take-off \bar{P}^n (panel b and d) for a single tethered (panel a–b) and three tethered device (panel c–d). The black line indicates one on one correspondence, and the dashed lines indicate the 20% error bands. In panel (a), the colors indicate the respective degree of freedom, and for each degree of freedom, its body response is normalised by the maximum predicted motion of the body. The power take off is normalised with $B_{p10} w^2 a^2$, where w is the radial wave frequency and a is the incident wave amplitude. (For interpretation of the references to color in this figure legend, the reader is referred to the Web version of this article.)

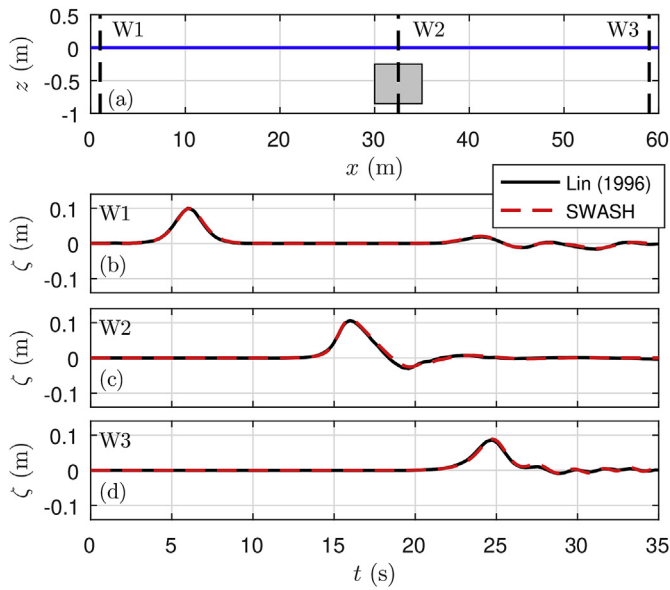


Fig. 11. Set-up of the solitary wave test case and snapshot of the free surface at $t = 10$ s (panel a), and the time series of the free-surface elevation at the three wave sensors (panel b–d). The black line indicates the solution of the 20 σ -layer model and VOF model of Lin (2006) (which are virtually indistinguishable), and the dashed red line indicates the solution of the 3 layer SWASH model. (For interpretation of the references to color in this figure legend, the reader is referred to the Web version of this article.)

simulations with 4 layers.

To summarize the findings for all water depths, Fig. 10 shows the results of the body response and mean power take-off for all simulations, and Table 1 shows the statistical metrics for the individual body motions (surge, heave, and pitch) and the mean power take-off. These results confirm that the simulations with $d = 30$ m are representative for all water depths. For both the single and three-tethered device, the agreement was best for the heave motion, followed by the surge and the pitch response. Although the individual motions of the device were occasionally predicted with significant inaccuracies, the power take-off and the dominant response of the device were reproduced with satisfactory accuracy, especially given the coarse vertical resolutions that were used.

4.3. Nonlinear waves

Following the test cases with linear waves, we aim to gain insight in the capabilities of the model for nonlinear conditions with larger wave amplitudes. For this purpose, we considered two test cases in which nonlinear waves interact with a submerged obstacle. The first test case considered the scattering of a solitary wave by a submerged pontoon (which is fixed in position). In the second test case we compared model results with a laboratory experiment of regular waves interacting with an idealised submerged floating breakwater (analogous to a submerged point absorber). For both test cases, the numerical simulations were performed with 3 layers, which is the minimum number of layers required to simulate the interactions of waves with submerged structures.

4.3.1. Scattering of a solitary wave by a submerged pontoon

Lin (2006) simulated the interaction of a solitary wave with a submerged pontoon using a σ -layer and Volume Of Fluid (VOF) based RANS model (see Fig. 11a for the test set-up). The domain had a length of 35 m with a still water depth of 1 m. The submerged object, with its centre located at $x = 32.5$ m, had a length of 5 m, a height of 0.4 m, and was positioned 0.25 m below the water surface. At the wavemaker, a solitary wave with a height of 0.1 m was generated. Both models of Lin (2006) gave near identical results despite their different vertical resolution (20 layers in case of the σ -layer model, and 130 meshes for the VOF model). To illustrate the capabilities of the SWASH model, we reproduced this test case with similar horizontal and temporal resolutions ($\Delta x = 0.05$ m, and $\Delta t = 0.01$ s), but with only 3 vertical layers.

SWASH predictions of the surface elevation were compared with the solution of Lin (2006) at three output locations (Fig. 11b–d). After generation, the solitary wave propagated towards the obstacle, where it arrived after about 12 s, and was partially reflected and transmitted. The reflected wave reached the first output location (W1) at $t \approx 22.5$ s, after which it was absorbed by the wavemaker. On top of the obstacle, the solitary wave deformed as it pitched forward, followed by a negative trough (Fig. 11b). The peak of the transmitted wave reached the final output location (W3) after $t \approx 24$ s, followed by some small oscillations (Fig. 11c). At all three output locations, the SWASH predicted surface elevation was in excellent agreement with the reference solution (with an average nE = 0.10 and MS = 0.99).

We note that a similar test case was used by Ma et al. (2016) to validate NHWAVE, a non-hydrostatic wave-flow model that they extended with the immersed boundary method to resolve the wave-structure interactions. They found a similar agreement between their

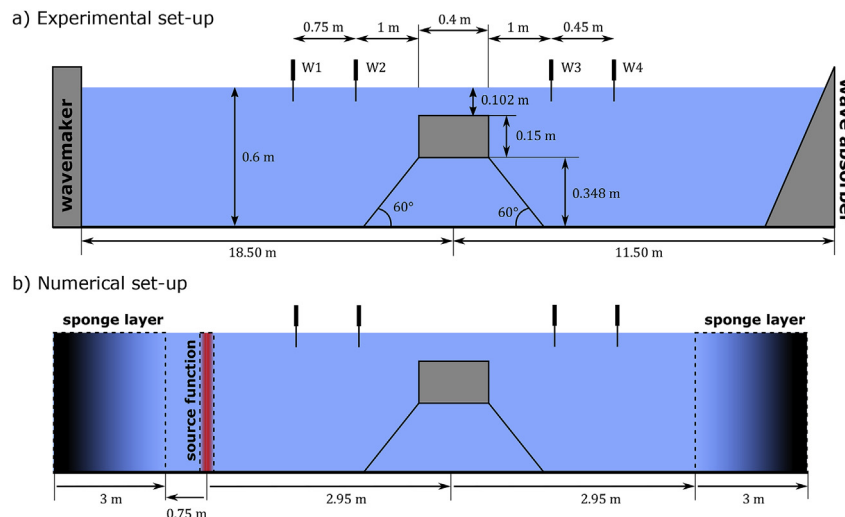


Fig. 12. Side view sketch (not to scale) of the experimental set-up (panel a) of Peng et al. (2013), and the numerical set-up (panel b).

non-hydrostatic model and a VOF model. However, in contrast to the results presented here, Ma et al. (2016) used 40 layers to simulate these dynamics (in order to capture the flow field around the obstacle). Given the fine vertical resolution, their computations likely required considerably larger computational resources as such detailed simulations are typically an order of magnitude slower compared to the three-layer simulations of this work. On the other hand, the three-layer simulations of this work do not capture the vertical flow structure. However, if the evolution of the solitary wave is of primary interest this work shows that a coarse vertical resolution is sufficient to capture such dynamics.

4.3.2. Wave interactions with a moored submerged obstacle

As a final test case, we compared model predictions with the laboratory experiment of Peng et al. (2013), who considered the interactions of a (nonlinear) regular wave with a submerged floating breakwater. Although this is not a wave energy device, it is directly analogous to a multi-tethered wave energy device (4 tethers in this case). This experiment was conducted in a 30 long wave flume with a (still) water depth of 0.6 m (see Fig. 12a for all relevant dimensions).

The positively buoyant pontoon ($m = 28.6$ kg, and $I_y = 0.435$ kg m²) was located roughly halfway down the flume and extended almost completely across the flume. To ensure that the 3D experiment can be regarded as a 2D test case, the body was moored using four carefully arranged steel chains that ensured symmetry in x and y -direction (refer to Peng et al., 2013, for more details). At the wavemaker, a regular wave with a height of 0.046 m and period of 1 s was generated. A wave absorber was positioned at the downwave end of the flume to minimise reflections. Waves were observed to break on top of the breakwater, illustrating the non-linearity of this test case.

To reproduce the experiment, SWASH was employed with a horizontal grid resolution of $\Delta x = 0.02$ m (corresponding to ≈ 70 points per wave length and 20 points per breakwater length), 3 layers in the vertical, and a time step of $\Delta t = 0.003$ s. Waves were generated inside the domain using a source function (Lin and Liu, 1999), and sponge layers (measuring approximately two wave lengths) were used at both ends of the numerical domain to minimise unwanted wave reflections (see Fig. 12b for a sketch of the numerical set-up). The target wave height was calibrated by matching the measured surge response of the breakwater. Following Ren et al. (2017), the mooring lines were modelled as stiff linear springs with $K_{pl0} = 1 \times 10^6$ N m⁻¹. To obtain a stable simulation for this stiff mooring line system, the Newmark

parameters were set at $\beta = 1/2$ and $\gamma = 1$. The simulation was run for a total duration of 35 s, including a spin-up time of about 15 s after which steady-state conditions were reached.

The predicted body motions agreed well with the measurements (Fig. 13a–c), both in terms of their temporal variation as their magnitude. The heave response was slightly under predicted, but the model did capture the local minima in heave that occurs between the two local maxima where $Z \approx 0$). Furthermore, the typical magnitude and variation of the mooring line forces were well reproduced (Fig. 13d–e). The model however failed to reproduce the local minima in the forces (especially for the mooring line on the leeward side of the body, Fig. 13e), which coincides with the local minima in the heave response (Fig. 13b). At the upwave side of the breakwater, where standing waves occurred due to the partial reflections of the incident wave at the body, the predicted surface elevations agreed well with the measurements (Fig. 14a–b). In contrast, the phasing of the predicted and measured surface elevations did not agree downwave of the breakwater, although the predicted wave height compared well (Fig. 14c–d). In the lee of the breakwater, the wave field was a combination of (partially) transmitted incident waves, including a secondary harmonic generated due to the wave-structure interactions (e.g., due to the reduced water depth on top of the breakwater), and waves radiated by the body motions.

A spectral analysis shows that at the first two sensors (W1–W2) the predicted magnitude and phase of the first wave component (at $f = 1$ Hz) were in reasonable agreement with the measurements (Fig. 14e–f). In the lee of the device, the discrepancies in the predicted magnitude and especially phase were typically larger for both the first and secondary harmonic (Fig. 14g–h), explaining the previously observed mismatch between the predicted and measured time series (Fig. 14c–d). To investigate if this mismatch is caused by the exclusion of the surge and pitch body motions when updating the flow grid, we compared an OpenFOAM – a VOF model – and a SWASH simulation for the same test case but without the body motions (i.e., solving the diffraction problem). This analysis shows that a 3-layer SWASH model captured the magnitude and phase of the primary harmonic in the lee of the (non-moving) obstacle, whereas a fine vertical resolution (100 layers) was required to also capture the phase of the secondary harmonic (see Appendix C). These findings suggest that the discrepancies between the model predictions and measurements observed in Fig. 14 are (at least in part) related to the coarse vertical resolution. Using a finer vertical resolution (100 layers) to reproduce the laboratory experiment

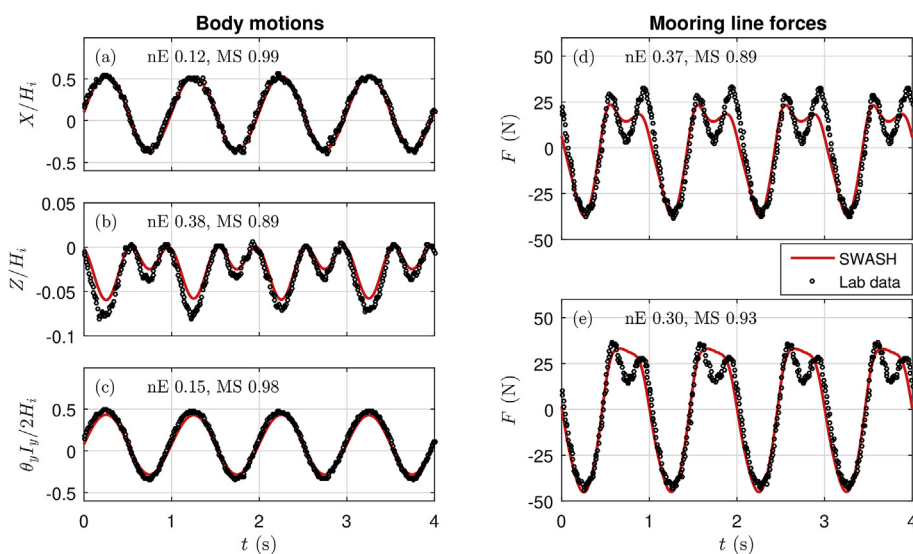


Fig. 13. Comparison between the predicted (red lines) and measured (black markers) normalised body motions (panel a–c) and mooring line forces (panel d–e) for a duration of 4 wave periods after steady-state conditions were reached. (For interpretation of the references to color in this figure legend, the reader is referred to the Web version of this article.)

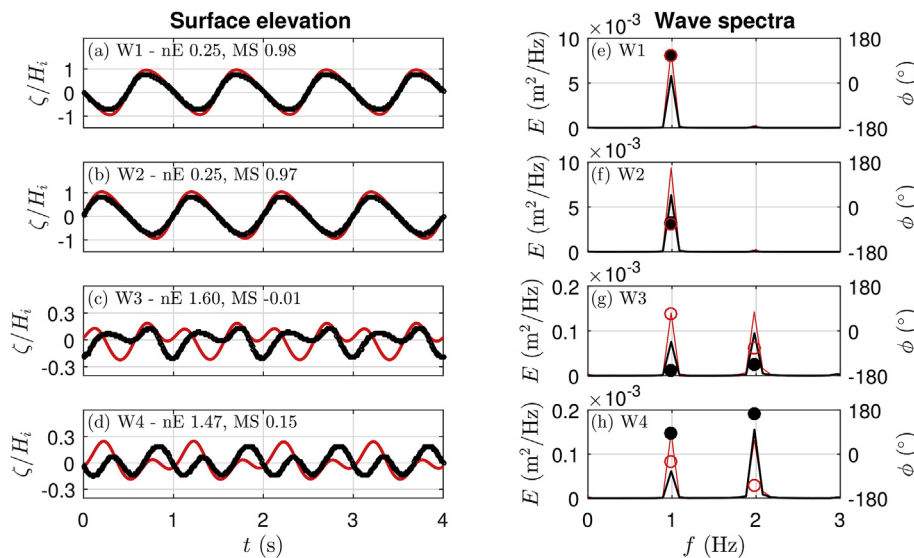


Fig. 14. Panel a–d: comparison between the predicted (red lines) and measured (black markers) normalised wave elevations (panel a–d) for a duration of 4 wave periods after steady-state conditions were reached. Panel e–g: predicted (red line and open circular marker) and measured (black line and filled circular marker) energy density spectra (lines – left axis) and phase (markers – right axis) of the surface elevation signals. Note that the phase is only shown for the primary wave frequency (1 Hz) and the second-harmonic (2 Hz). (For interpretation of the references to color in this figure legend, the reader is referred to the Web version of this article.)

(including the body motions) did indeed alter the model predictions. However, it did not improve the model-data agreement in the lee of the device (not shown). This thereby suggests that the mismatch between the predicted and measured surface elevation in the lee of the device (Fig. 13c–d) is related to both the coarse vertical resolution and the exclusion of the surge and pitch body motions when updating the flow grid.

5. Discussion

In this work we developed a new approach to simulate the evolution of the waves and their interactions with a submerged point absorber. The primary objective was to resolve both the nonlinear evolution of the waves and the wave-induced response of a submerged point absorber at the scale of a realistic coastal region. The submerged body was directly included within the computational flow domain, and a fully dynamic coupling between the body and flow equations was implemented to capture the wave-structure interactions. The relevant kinematic boundary conditions were directly imposed at the hull of the body, and we did not account for the horizontal motions and the rotations of the body in the flow grid. Although this formally restricts the method to small body motions relative to the flow grid, this allows a simple and relatively efficient numerical approach as it does not rely on more involved techniques (e.g., the immersed boundary method) to account for the lateral and rotational body motions in the flow grid.

Despite this model limitation, the results of the test cases with linear waves (Section 4.2) demonstrated the potential of the model to capture the dominant response of a submerged point absorber. Importantly, the model captured these dynamics with relatively coarse vertical resolutions (ranging only 3 to 7 vertical layers). For all simulations, only one layer was positioned above the body, one layer was running through the body, and all remaining layers were located below the body. Furthermore, the model was also shown to be able to handle nonlinear wave conditions, as exemplified by the satisfactory agreement for two test cases presented in Section 4.3. Although the small motion assumption and the coarse vertical resolution introduced some inaccuracies in the magnitude and phase of the wave components in the lee of the submerged breakwater, the overall agreement between the predicted and measured wave field, body motions, and mooring line forces was encouraging (Figs. 13 and 14) – especially given that only

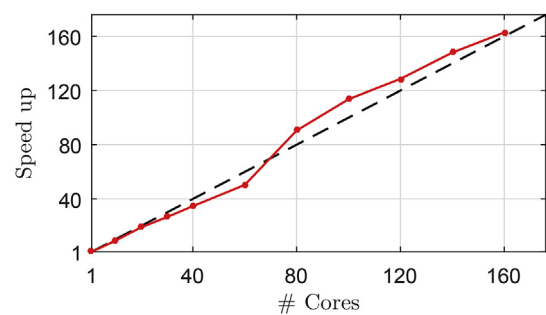


Fig. 15. Parallel scaling of the model on the Magnus system. The line with the markers indicates the model speed-up, and the dashed line illustrates a linear speed-up (which means that, for example, the simulation time is halved when double the amount of cores is used).

three layers were used for this particular test case. The use of such a relatively coarse vertical resolution implies a significant reduction in computational resources, especially compared to CFD type simulations that reproduced the same complex test case (Peng et al., 2013; Ren et al., 2017). For example, Ren et al. (2017) reported a Smoothed Particle Hydrodynamic simulation that took 7 h on 4 cores (INTEL Core i7-4790 CPU@3.6 GHz) for a domain length of 7.2 m and a simulation duration of 20 s. In comparison, a SWASH simulation of the same test case took only 1 min on a single core (INTEL Core i7-6700 CPU@ 3.6 GHz) for a domain length of 12.7 m and a duration of 35 s, highlighting its efficiency in solving the interactions between waves and moving bodies.

Furthermore, the model showed excellent parallel scaling on Magnus, a 1097 TeraFLOPS high-performance computing facility that is part of the Pawsey Supercomputing Centre located in Western Australia. For example, the model showed a linear speed-up for up to 160 cores for a three layer diffraction simulation that spans 896×156 cells (Fig. 15). Although an iterative procedure was required for each time step of the simulation when body motions were included, it typically converged in less than five iterations. This does imply additional computational costs; however, due to the small number of iterations the simulations typically took on average about 3 times as long to run compared to a simulation without body motions. The coarse vertical resolutions that were sufficient to capture the wave dynamics and

wave-structure interactions demonstrate that large scale applications (spanning $\mathcal{O}(10 \times 10)$ wave lengths and $\mathcal{O}(100)$ wave periods) are feasible on high-performance computing facilities.

Part of the model efficiency can be attributed to the simplification of representing the free-surface as a single-valued function (in contrast with, for example, the more involved VOF method). This however does imply that the model does not account for processes such as the overturning of the free-surface (e.g., in plunging waves), the entrainment of air, and splashing of the water. Such phenomena are important when considering the survivability of a WEC during extreme conditions (when devices are not likely extracting wave energy). When producing power during operational conditions these processes are however not expected to dominate the response of the devices. Therefore, if one is primarily interested in the impact of wave farms at coastal scales – which ultimately is the aim of the presented modelling approach – these missing processes will not likely adversely impact the accuracy of the model.

For large-scale applications, the primary advantage of the proposed model compared to existing tools is that it accounts for most processes that are relevant when considering the impact of a wave farm. This includes not only the evolution of waves and their interactions with the wave farm, but also wave-generated currents in the nearshore. Although the model does not account for the resulting sediment transport, current patterns have successfully been used as a proxy for the mode of shoreline response (i.e., erosive or accretive) in the lee of coastal structures (e.g., Ranasinghe et al., 2010) and can likely also be used as a proxy to assess the coastal impact of wave farms.

The present work focussed on simulating the interactions between waves and a submerged floating obstacle. However, it is important to emphasise that the general numerical methodology can be extended to include other type of devices (e.g., floating point absorbers, bottom-mounted flaps, and oscillating water columns). Several previous authors have presented extensions of the non-hydrostatic approach to account for the presence of floating bodies. For example, Ma et al. (2016) and Orzech et al. (2016) simulated such wave-structure interactions using the immersed boundary method, and Rijnsdorp and Zijlema (2016) simulated these using a methodology that is similar to the one presented in this work. Although these studies did not consider the dynamic response of the floating bodies, this can be relatively straightforwardly included using the concepts presented in this work. In this manner, future work can extend our current modelling capabilities towards predicting the far-field impact of arrays of generic WECs, assisting the design of the optimal placement and configuration of future wave energy farms. Furthermore, the methodology is not restricted to submerged wave-energy-converters, but can be applied to any type of submerged structure (e.g., submerged floating breakwaters).

6. Conclusions

In this work, we have presented a new approach to simulate the

Appendix A. Statistical measures

To quantify the model convergence and model accuracy, we computed three statistical metrics: the normalised root-mean-square-error (nE), the relative bias (RB), and the Murphy skill (MS) score. The nE was computed as,

$$\text{nE} = \frac{\sqrt{\frac{1}{N} \sum_{i=1}^N (Q^i - Q_R^i)^2}}{\sigma_{Q_R}}, \quad (\text{A.1})$$

where Q is the model prediction and Q_R is the reference solution in a sample size of N , σ indicates the standard deviation, and the brackets $\langle \dots \rangle$ indicates averaging. The relative bias was computed as (e.g., Van der Westhuysen, 2010),

interactions between waves and submerged floating bodies based on the non-hydrostatic wave-flow model SWASH. The primary objective of this work was to resolve both the nonlinear evolution of the waves and the wave-induced response of a submerged point absorber at the scale of a realistic coastal region. To validate the developed model, we considered several test cases including both linear and nonlinear waves, which also provided insight into the capabilities of the developed approach.

For linear wave conditions, model results were compared to an analytical solution (based on the potential flow equations) for the diffraction problem, radiation problem, and the dynamic response of a (single and three tethered) submerged cylindrical point-absorber. For a range of water depths and wave periods, the model captured the dominant response and power take-off of the point absorber with satisfactory accuracy.

Subsequently, the model was validated for a solitary wave and regular wave interacting with a submerged floating pontoon (or breakwater). For both these non-linear test cases, model predictions were in satisfactory agreement with the reference solutions (a previous numerical modelling study and a laboratory experiment, respectively) in terms of the wave elevation, wave-induced body motions, and mooring line forces.

Importantly, the model captured all of these dynamics with a relative coarse vertical resolution (ranging only 3 to 7 vertical layers). Combined with the excellent scalability on high-performance computing facilities, such coarse resolutions show that the model is suited to simulate the wave dynamics and wave-structure interactions at realistic field scales of $\sim \mathcal{O}(1 \times 1)$ km. This work thereby presents the first step towards the development of a new tool to simulate the non-linear evolution of waves and their interactions with WECs at the scale of a realistic coastal region.

Acknowledgements

Funding for this work was provided by the Australian Renewable Energy Agency (ARENA) as part of ARENA's Research and Development Programme in a joint project with Carnegie Clean Energy (grant number 2015RND086), and was supported by resources provided by the Pawsey Supercomputing Centre with funding from the Australian Government and the Government of Western Australia. We thank Wei Peng for sharing the laboratory data, and Nataliia Sergiienko for making her Matlab code to solve the eigenfunction expansion problem publicly available via ResearchGate. We also thank Christophe Gaudin, Scott Draper, Ashkan Rafiee, Hugh Wolgamot, Jana Orszaghova, and Marcel Zijlema for fruitful discussions that benefited this work; and Lifan Chen and Feifei Tong for their help running OpenFoam. Finally, we greatly appreciate the time and effort of two anonymous reviewers whose feedback improved this paper.

$$RB = \frac{\frac{1}{N} \sum_i^N (Q^i - Q_R^i)}{\frac{1}{N} \sum_i^N Q_R^i}, \quad (\text{A.2})$$

and indicates to what extent the model predictions over estimate (positive RB values) or under predict (negative RB values) the reference solution. The skill score was computed as (Murphy, 1988),

$$MS = 1 - \frac{\sum_i^N (Q^i - \overline{Q_R^i})^2}{\sum_i^N (Q_R^i - \overline{Q_R^i})^2}, \quad (\text{A.3})$$

where the overbar indicates averaging. With this skill metric, a score of 1 indicates perfect agreement and a score below zero indicates that the model predictive ability is worse than mean of the reference solution (e.g., Ralston et al., 2010; Hansen et al., 2015).

Appendix B. Frequency domain solution of the body response

Assuming small amplitude waves and small body motions, a frequency domain solution can be derived to compute the wave-induced response of a body (e.g., Alves, 2016). For a generic body that moves in heave, surge and pitch, this solution can be written as (e.g., Sergiienko et al., 2018),

$$\mathbf{A}(\omega) \frac{\partial^2 \hat{\xi}}{\partial t^2} + (\mathbf{B}_{\text{pto}} + \mathbf{B}(\omega)) \frac{\partial \hat{\xi}}{\partial t} + \mathbf{K}_{\text{pto}} \hat{\xi} = \hat{\mathbf{F}}_h, \quad (\text{B.1})$$

where $\hat{\xi} = [\hat{X}, \hat{Z}, \hat{\theta}_y]^T$ represents the vector of the body motions, and $\hat{\cdot}$ indicates the complex amplitude,

$$\mathbf{A}(\omega) = \begin{bmatrix} m + a_{11} & 0 & a_{13} \\ 0 & m + a_{22} & 0 \\ a_{31} & 0 & I_y + a_{33} \end{bmatrix}, \quad \mathbf{B}(\omega) = \begin{bmatrix} b_{11} & 0 & b_{13} \\ 0 & b_{22} & 0 \\ b_{31} & 0 & b_{33} \end{bmatrix}, \quad (\text{B.2})$$

and a_{ij} and b_{ij} represent the frequency dependent hydrodynamic coefficients, where the subscripts distinct between surge ($i = j = 1$) heave ($i = j = 2$), and pitch ($i = j = 3$). The remaining parameters, \mathbf{K}_{pto} and \mathbf{B}_{pto} depend upon the mooring line arrangement. For a single tethered cylindrical device, these parameters read,

$$\mathbf{K}_{\text{pto}} = \begin{bmatrix} \frac{C_{\text{pto}}}{l} & 0 & -\frac{C_{\text{pto}}h}{l} \\ 0 & K_{\text{pto}} & 0 \\ -\frac{C_{\text{pto}}h}{l} & 0 & \frac{C_{\text{pto}}h}{l}(l+h) \end{bmatrix}, \quad \mathbf{B}_{\text{pto}} = \begin{bmatrix} 0 & 0 & 0 \\ 0 & B_{\text{pto}} & 0 \\ 0 & 0 & 0 \end{bmatrix}, \quad (\text{B.3})$$

where l is the initial length of the mooring line, and h is half the height of the cylinder (i.e., the distance from the mooring line attachment point to the centre of gravity of the cylinder). For a three tethered device, with all tethers pointing towards the centre of gravity of the cylinder and equally spaced in the horizontal plane (forming edges of the cuboidal vertex, see Fig. 2), these parameters read (Sergiienko et al., 2018),

$$\mathbf{K}_{\text{pto}} = \begin{bmatrix} \frac{3}{2} \sin^2 \alpha_V \left(K_{\text{pto}} - \frac{C_{\text{pto}}}{3 \cos \alpha_V} \right) + \frac{C_{\text{pto}}}{l \cos \alpha_V} & 0 & -\frac{C_{\text{pto}}h}{l} \\ 0 & 3 \cos^2 \alpha_V \left(K_{\text{pto}} - \frac{C_{\text{pto}}}{3 \cos \alpha_V} \right) + \frac{C_{\text{pto}}}{l \cos \alpha_V} & 0 \\ -\frac{C_{\text{pto}}h}{l} & 0 & \frac{C_{\text{pto}}h(l+h)(\cos^2 \alpha_V + 1)}{2 \cos \alpha_V} \end{bmatrix}, \quad (\text{B.4})$$

$$\mathbf{B}_{\text{pto}} = \begin{bmatrix} \frac{3}{2} B_{\text{pto}} \sin^2 \alpha_V & 0 & 0 \\ 0 & 3 B_{\text{pto}} \cos^2 \alpha_V & 0 \\ 0 & 0 & 0 \end{bmatrix}, \quad (\text{B.5})$$

where α_V is the vertical angle of the mooring line with the centre of gravity of the cylinder (see Fig. 2).

The solution of the system of equations (Eq. (B.1)) determines the response of the moored body. Based on the linear response, the mean power take-off can be computed as (e.g., Alves, 2016),

$$\bar{P} = \frac{1}{2} \omega^2 \hat{\xi}^T \mathbf{B}_{\text{pto}} \hat{\xi}^*, \quad (\text{B.6})$$

where \dots^* indicates the complex conjugate.

Appendix C. SWASH - OpenFOAM comparison

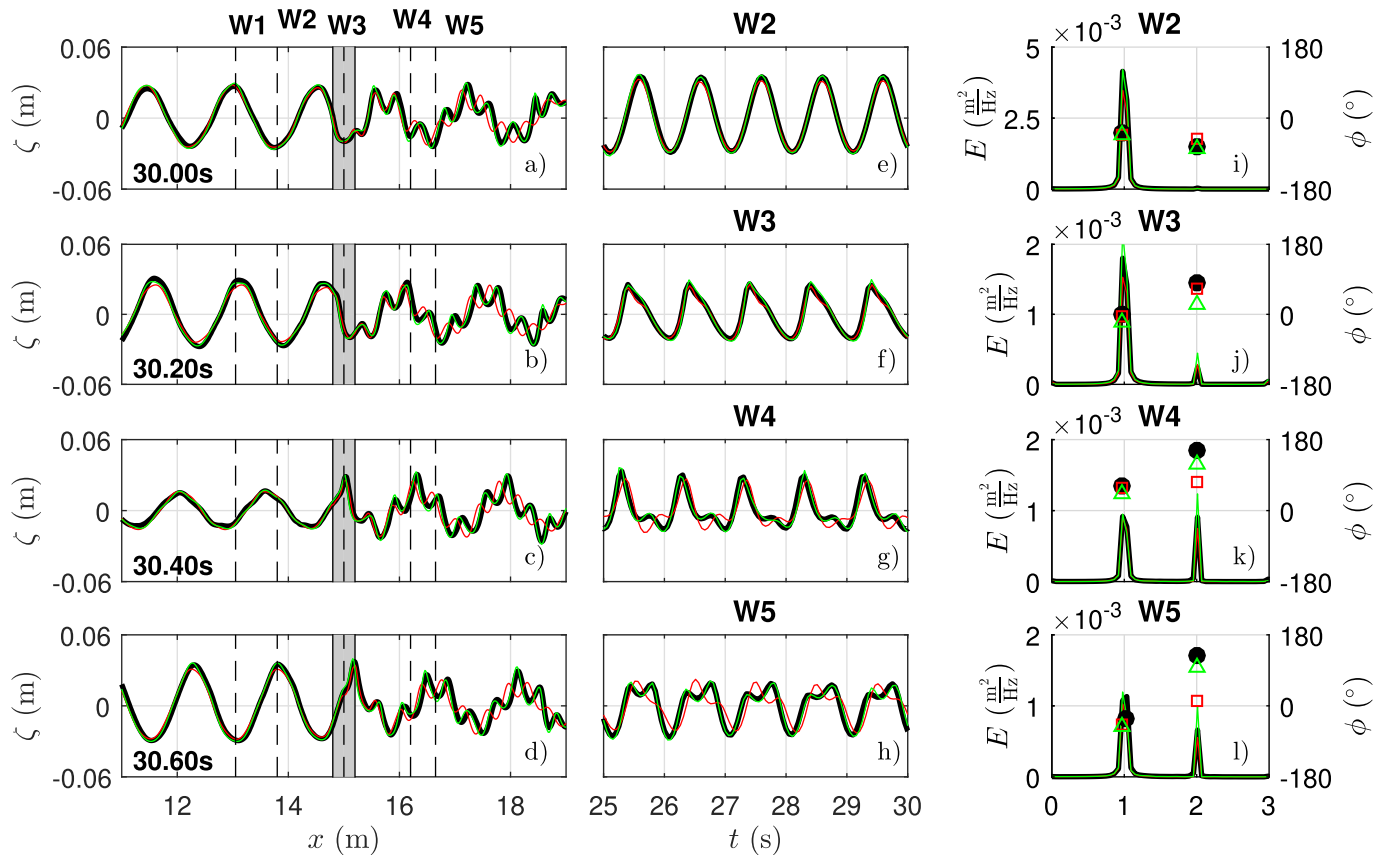


Fig. C.1. OpenFOAM (black line and markers) and SWASH (red line and markers, 3-layer simulation; and green line and markers, 100-layer simulation) comparison for the interaction between a regular wave and a fixed submerged floating breakwater. Panel a–d show a snapshot of the surface elevation near the obstacle at four different time steps (as indicated in each panel). In these panels, the dashed vertical lines indicate the location of the wave sensors (labelled in panel a), and the shaded grey area indicates the location of the breakwater. Panel e–h show the time-series of the surface at 4 sensor locations (W2–W5) for a duration of 5 wave periods after spin-up. Panel i–l show the energy density spectra (left axis, full line) and the phase (markers) of the surface elevation at these 4 wave sensors. In these plots, the phase is only shown for the primary wave frequency (1 Hz) and the second-harmonic (2 Hz).

To investigate the mismatch between the SWASH predictions and laboratory measurements (Peng et al., 2013) of the surface elevation signals in the lee of the submerged floating breakwater (section 4.3.2), we compared an OpenFOAM (including the IHFoam toolbox to generate and absorb waves; Higuera et al., 2013, 2014) with a SWASH simulation for the same test case that excludes the body motions. The OpenFOAM simulation was run with a horizontal grid resolution of $\Delta x = 1$ cm, and a vertical grid resolution of $\Delta z = 0.5 - 1$ cm (with the finest grid resolution near the free-surface). SWASH was run with the same horizontal resolution, and with both 3 layers and 100 layers (the latter resulting in a vertical resolution that is comparable to the OpenFOAM simulation). To minimise the influence of (re-)reflections at the side boundaries in the OpenFOAM simulations (related to inaccuracies introduced by the active wave absorption in IHFoam), we considered a longer domain with a length of 30 m, with the obstacle located at $x = 15$ m.

The comparison between SWASH and OpenFOAM was best for the 100 layer simulation, in which case the free-surface profile near the obstacle (Fig. C1a–d), and the surface elevation time-series at the wave sensors (Fig. C1e–h) were in good agreement. A spectral analysis confirms that both the magnitude and the phase of the primary wave component ($f = 1$ Hz) agreed at sensors W2–W5. The same holds for the super-harmonic wave component ($f = 2$ Hz) that is generated through the interactions between the waves and the obstacle, although a relatively small phase difference ($\Delta\phi \approx 38^\circ$) was observed between the 100-layer SWASH and OpenFOAM solution in the lee and above the obstacle (Fig. C1j–l). Despite this phase difference, the surface-elevation signals compared well at sensors W3 and W4. In contrast, the surface-elevation predicted by the 3-layer SWASH simulation showed larger discrepancies in the lee of the device, and the spectral analysis shows that this can be attributed to a larger $\Delta\phi$ ($\approx 80^\circ$) between the SWASH and OpenFOAM super-harmonic wave component (as the phase of the primary component was nearly identical). Given that the 100-layer SWASH simulation captured the surface elevation signals in the lee of the obstacle, these results indicate that this mismatch is a result of the coarse vertical resolution.

References

- Abanades, J., Greaves, D., Iglesias, G., 2014. Coastal defence through wave farms. *Coast. Eng.* 91, 299–307.
- Agamloh, E.B., Wallace, A.K., von Jouanne, A., 2008. Application of fluid–structure interaction simulation of an ocean wave energy extraction device. *Renew. Energy* 33, 748–757.
- Ai, C., Jin, S., 2012. A multi-layer non-hydrostatic model for wave breaking and run-up. *Coast. Eng.* 62, 1–8.
- Alves, M., 2016. Frequency-domain models. In: Folley, M. (Ed.), *Numerical Modelling of Wave Energy Converters: State-of-the-art Techniques for Single Devices and Arrays*. Elsevier, pp. 11–30 (chapter 2).
- Babarit, A., 2013. On the park effect in arrays of oscillating wave energy converters.

- Renew. Energy 58, 68–78.
- Babarit, A., Hals, J., Muliawan, M., Kurniawan, A., Moan, T., Krokstad, J., 2012. Numerical benchmarking study of a selection of wave energy converters. *Renew. Energy* 41, 44–63.
- Beels, C., Troch, P., De Backer, G., Vantorre, M., De Rouck, J., 2010a. Numerical implementation and sensitivity analysis of a wave energy converter in a time-dependent mild-slope equation model. *Coast. Eng.* 57, 471–492.
- Beels, C., Troch, P., De Visch, K., Kofoed, J.P., De Backer, G., 2010b. Application of the time-dependent mild-slope equations for the simulation of wake effects in the lee of a farm of Wave Dragon wave energy converters. *Renew. Energy* 35, 1644–1661.
- Bergillos, R.J., López-Rauz, A., Medina-López, E., Moñino, A., Ortega-Sánchez, M., 2018. The role of wave energy converter farms on coastal protection in eroding deltas, Guadalfeo, southern Spain. *J. Clean. Prod.* 171, 356–367.
- Bharath, A., Nader, J.R., Penesis, I., Macfarlane, G., 2018. Nonlinear hydrodynamic effects on a generic spherical wave energy converter. *Renew. Energy* 118, 56–70.
- Borazjani, I., Ge, L., Sotiropoulos, F., 2008. Curvilinear immersed boundary method for simulating fluid structure interaction with complex 3D rigid bodies. *J. Comput. Phys.* 227, 7587–7620.
- Casulli, V., Stelling, G.S., 1998. Numerical simulation of 3D quasi-hydrostatic, free-surface flows. *J. Hydraul. Eng.* 124, 678–686.
- Chang, G., Ruehl, K., Jones, C., Roberts, J., Chartrand, C., 2016. Numerical modeling of the effects of wave energy converter characteristics on nearshore wave conditions. *Renew. Energy* 89, 636–648.
- Chen, W., Dolgunsteva, I., Savin, A., Zhang, Y., Li, W., Svensson, O., Leijon, M., 2017. Numerical modelling of a point-absorbing wave energy converter in irregular and extreme waves. *Appl. Ocean Res.* 63, 90–105.
- Crespo, A., Altomare, C., Domínguez, J., González-Cao, J., Gómez-Gesteira, M., 2017. Towards simulating floating offshore oscillating water column converters with Smoothed Particle Hydrodynamics. *Coast. Eng.* 126, 11–26.
- Day, A., Babarit, A., Fontaine, A., He, Y.P., Kraskowski, M., Murai, M., Penesis, I., Salvatore, F., Shin, H.K., 2015. Hydrodynamic modelling of marine renewable energy devices: a state of the art review. *Ocean Eng.* 108, 46–69.
- Devolder, B., Stratigaki, V., Troch, P., Rauwoens, P., 2018. CFD simulations of floating point absorber wave energy converter arrays subjected to regular waves. *Energies* 11, 641.
- Engsig-Karup, A., Bingham, H., Lindberg, O., 2009. An efficient flexible-order model for 3D nonlinear water waves. *J. Comput. Phys.* 228, 2100–2118.
- Folley, M., 2016. Numerical Modelling of Wave Energy Converters: State-of-the-art Techniques for Single Devices and Arrays. Elsevier.
- García-Medina, G., Özkan-Haller, H.T., Holman, R.A., Ruggiero, P., 2017. Large runup controls on a gently sloping dissipative beach. *J. Geophys. Res.: Oceans* 122, 5998–6010.
- Gomes, E.R., Mulligan, R.P., Brodie, K.L., McNinch, J.E., 2016. Bathymetric control on the spatial distribution of wave breaking in the surf zone of a natural beach. *Coast. Eng.* 116, 180–194.
- Gonzalez-Santamaria, R., Zou, Q.P., Pan, S., 2013. Impacts of a wave farm on waves, currents and coastal morphology in south west England. *Estuar. Coast* 38, 1–14.
- Greenwood, C., Christie, D., Venugopal, V., Morrison, J., Vogler, A., 2016. Modelling performance of a small array of wave energy converters: comparison of spectral and Boussinesq models. *Energy* 113, 258–266.
- Hansen, 1956. Theorie zur Errechnung des Wasserstandes und der Strömungen in Randmeeren nebst Anwendungen. *Tellus* 8, 289–300.
- Hansen, J.E., Raubenheimer, B., List, J.H., Elgar, S., 2015. Modeled alongshore circulation and force balances onshore of a submarine canyon. *J. Geophys. Res.: Oceans* 120, 1887–1903.
- Higuera, P., Lara, J.L., Losada, I.J., 2013. Realistic wave generation and active wave absorption for Navier–Stokes models. *Coast. Eng.* 71, 102–118.
- Higuera, P., Lara, J.L., Losada, I.J., 2014. Three-dimensional interaction of waves and porous coastal structures using OpenFOAM®. Part I: formulation and validation. *Coast. Eng.* 83, 243–258.
- Iglesias, G., Carballo, R., 2014. Wave farm impact: the role of farm-to-coast distance. *Renew. Energy* 69, 375–385.
- Jiang, S.C., Gou, Y., Teng, B., 2014a. Water wave radiation problem by a submerged cylinder. *J. Eng. Mech.* 140, 06014003.
- Jiang, S.C., Gou, Y., Teng, B., Ning, D.Z., 2014b. Analytical solution of a wave diffraction problem on a submerged cylinder. *J. Eng. Mech.* 140, 225–232.
- Lam, D.C.L., Simpson, R.B., 1976. Centered differencing and the box scheme for diffusion convection problems. *J. Comput. Phys.* 22, 486–500.
- Lauder, B.E., Spalding, D.B., 1974. The numerical computation of turbulent flows. *Comput. Meth. Appl. Mech. Eng.* 3, 269–289.
- Li, Y., Yu, Y.H., 2012. A synthesis of numerical methods for modeling wave energy converter-point absorbers. *Renew. Sustain. Energy Rev.* 16, 4352–4364.
- Lin, P., 2006. A multiple-layer σ -coordinate model for simulation of wave–structure interaction. *Comput. Fluids* 35, 147–167.
- Lin, P., Liu, P.L.F., 1999. Internal wave-maker for Navier–Stokes equations models. *Journal of Waterway, Port, Coast. Ocean Eng.* 125, 207–215.
- Ma, G., Farahani, A.A., Kirby, J.T., Shi, F., 2016. Modeling wave-structure interactions by an immersed boundary method in a σ -coordinate model. *Ocean Eng.* 125, 238–247.
- Ma, G., Shi, F., Kirby, J.T., 2012. Shock-capturing non-hydrostatic model for fully dispersive surface wave processes. *Ocean Model.* 43–44, 22–35.
- Mavroukas, S., McIver, P., 1997. Comparison of methods for computing hydrodynamic characteristics of arrays of wave power devices. *Appl. Ocean Res.* 19, 283–291.
- Millar, D., Smith, H., Reeve, D., 2007. Modelling analysis of the sensitivity of shoreline change to a wave farm. *Ocean Eng.* 34, 884–901.
- Murphy, A.H., 1988. Skill scores based on the mean square error and their relationships to the correlation coefficient. *Mon. Weather Rev.* 116, 2417–2424.
- Newmark, N.M., 1959. A method of computation for structural dynamics. *J. Eng. Mech. Div.* 85, 67–94.
- Orzech, M.D., Shi, F., Veeramony, J., Bateman, S., Calantoni, J., Kirby, J.T., 2016. Incorporating floating surface objects into a fully dispersive surface wave model. *Ocean Model.* 102, 14–26.
- Özkan-Haller, H.T., Haller, M.C., McNatt, J.C., Porter, A., Lenee-Bluhm, P., 2017. Analyses of wave scattering and absorption produced by WEC arrays: physical/numerical experiments and model assessment. In: Yang, Z., Copping, A. (Eds.), *Marine Renewable Energy*. Springer International Publishing, pp. 71–97.
- Peng, W., Lee, K.H., Shin, S.H., Mizutani, N., 2013. Numerical simulation of interactions between water waves and inclined-moored submerged floating breakwaters. *Coast. Eng.* 82, 76–87.
- Radder, A., Dingemans, M., 1985. Canonical equations for almost periodic, weakly nonlinear gravity waves. *Wave Motion* 7, 473–485.
- Ralston, D.K., Geyer, W.R., Lerczak, J.A., Scully, M., 2010. Turbulent mixing in a strongly forced salt wedge estuary. *J. Geophys. Res.* 115, C12024.
- Ranasinghe, R., Larson, M., Savioli, J., 2010. Shoreline Response to a Single Shore-parallel Submerged Breakwater.
- Ransley, E.J., Greaves, D., Raby, A., Simmonds, D., Hann, M., 2017. Survivability of wave energy converters using CFD. *Renew. Energy* 109, 235–247.
- Ren, B., He, M., Li, Y., Dong, P., 2017. Application of smoothed particle hydrodynamics for modeling the wave-moored floating breakwater interaction. *Appl. Ocean Res.* 67, 277–290.
- Rijnsdorp, D.P., Ruessink, G., Zijlema, M., 2015. Infragravity-wave dynamics in a barred coastal region, a numerical study. *J. Geophys. Res.: Oceans* 120, 4068–4089.
- Rijnsdorp, D.P., Smit, P.B., Zijlema, M., Reniers, A.J., 2017. Efficient non-hydrostatic modelling of 3D wave-induced currents using a subgrid approach. *Ocean Model.* 116, 118–133.
- Rijnsdorp, D.P., Zijlema, M., 2016. Simulating waves and their interactions with a restrained ship using a non-hydrostatic wave-flow model. *Coast. Eng.* 114, 119–136.
- Sergienko, N., Cazzolato, B., Ding, B., Hardy, P., Arjomandi, M., 2017. Performance comparison of the floating and fully submerged quasi-point absorber wave energy converters. *Renew. Energy* 108, 425–437.
- Sergienko, N., Rafiee, A., Cazzolato, B., Ding, B., Arjomandi, M., 2018. Feasibility study of the three-tether axisymmetric wave energy converter. *Ocean Eng.* 150, 221–233.
- Smagorinsky, J., 1963. General circulation experiments with the primitive equations. *Mon. Weather Rev.* 91, 99–164.
- Smith, H.C.M., Pearce, C., Millar, D.L., 2012. Further analysis of change in nearshore wave climate due to an offshore wave farm: an enhanced case study for the Wave Hub site. *Renew. Energy* 40, 51–64.
- Stansby, P.K., Zhou, J.G., 1998. Shallow-water flow solver with non-hydrostatic pressure: 2D vertical plane problems. *Int. J. Numer. Meth. Fluid.* 28, 541–563.
- Stelling, G., Zijlema, M., 2003. An accurate and efficient finite-difference algorithm for non-hydrostatic free-surface flow with application to wave propagation. *Int. J. Numer. Meth. Fluid.* 43, 1–23.
- Stelling, G.S., Duinmeijer, S.P.A., 2003. A staggered conservative scheme for every Froude number in rapidly varied shallow water flows. *Int. J. Numer. Meth. Fluid.* 43, 1329–1354.
- Stratigaki, V., Troch, P., Stallard, T., Forehand, D., Kofoed, J., Folley, M., Benoit, M., Babarit, A., Kirkegaard, J., 2014. wave basin experiments with large wave energy converter arrays to study interactions between the converters and effects on other users in the sea and the coastal area. *Energies* 7, 701–734.
- Troch, P., Stratigaki, V., 2016. Phase-resolving wave propagation array models. In: Folley, M. (Ed.), *Numerical Modelling of Wave Energy Converters: State-of-the-art Techniques for Single Devices and Arrays*. Academic Press, pp. 191–216.
- Van der Westhuysen, A.J., 2010. Modeling of depth-induced wave breaking under finite depth wave growth conditions. *J. Geophys. Res.: Oceans* 115.
- Van Kan, J., 1986. A second-order accurate pressure-correction scheme for viscous incompressible flow. *SIAM J. Sci. Stat. Comput.* 7, 870–891.
- Verbrugge, T., Stratigaki, V., Troch, P., Rabussier, R., Kortenhaus, A., 2017. A comparison study of a generic coupling methodology for modeling wake effects of wave energy converter arrays. *Energies* 10, 1697.
- Wolgamot, H., Taylor, P., Eatock Taylor, R., 2012. The interaction factor and directionality in wave energy arrays. *Ocean Eng.* 47, 65–73.
- Wolgamot, H.A., Fitzgerald, C.J., 2015. Nonlinear hydrodynamic and real fluid effects on wave energy converters. *Proc. IME J. Power Energy* 229, 772–794.
- Yamazaki, Y., Kowalik, Z., Cheung, K.F., 2009. Depth-integrated, non-hydrostatic model for wave breaking and run-up. *Int. J. Numer. Meth. Fluid.* 61, 473–497.
- Yu, Y., Xie, F., Yan, H., Constantinides, Y., Oakley, O., Karniadakis, G.E., 2015. Suppression of vortex-induced vibrations by fairings: a numerical study. *J. Fluid Struct.* 54, 679–700.
- Zijlema, M., Stelling, G., Smit, P., 2011. SWASH: an operational public domain code for simulating wave fields and rapidly varied flows in coastal waters. *Coast. Eng.* 58, 992–1012.
- Zijlema, M., Stelling, G.S., 2005. Further experiences with computing non-hydrostatic free-surface flows involving water waves. *Int. J. Numer. Meth. Fluid.* 48, 169–197.
- Zijlema, M., Stelling, G.S., 2008. Efficient computation of surf zone waves using the nonlinear shallow water equations with non-hydrostatic pressure. *Coast. Eng.* 55, 780–790.